processes

MDPI

Review

Hydrogen Production Through Newly Developed Photocatalytic Nanostructures and Composite Materials

Amra Bratovčić [1,*] and Vesna Tomašić [2,*]

[1] Department of Physical Chemistry and Electrochemistry, Faculty of Technology, University of Tuzla, Urfeta Vejzagića 8, 75000 Tuzla, Bosnia and Herzegovina
[2] Department of Reaction Engineering and Catalysis, Faculty of Chemical Engineering and Technology, University of Zagreb, Marulićev trg 19, 10000 Zagreb, Croatia
* Correspondence: amra.bratovcic@untz.ba (A.B.); vtomas@fkit.hr or vtomas@fkit.unizg.hr (V.T.)

Abstract: Photocatalytic hydrogen (H_2) production offers a promising solution to energy shortages and environmental challenges by converting solar energy into chemical energy. Hydrogen, as a versatile energy carrier, can be generated through photocatalysis under sunlight or via electrolysis powered by solar or wind energy. However, the advancement of photocatalysis is hindered by the limited availability of effective visible light-responsive semiconductors and the challenges of charge separation and transport. To address these issues, researchers are focusing on the development of novel nanostructured semiconductors and composite materials that can enhance photocatalytic performance. In this paper, we provide an overview of the advanced photocatalytic materials prepared so far that can be activated by sunlight, and their efficiency in H_2 production. One of the key strategies in this research area concerns improving the separation and transfer of electron–hole pairs generated by light, which can significantly boost H_2 production. Advanced hybrid materials, such as organic–inorganic hybrid composites consisting of a combination of polymers with metal oxide photocatalysts, and the creation of heterojunctions, are seen as effective methods to improve charge separation and interfacial interactions. The development of Schottky heterojunctions, Z-type heterojunctions, p–n heterojunctions from nanostructures, and the incorporation of nonmetallic atoms have proven to reduce photocorrosion and enhance photocatalytic efficiency. Despite these advancements, designing efficient semiconductor-based heterojunctions at the atomic scale remains a significant challenge for the realization of large-scale photocatalytic H_2 production. In this review, state-of-the-art advancements in photocatalytic hydrogen production are presented and discussed in detail, with a focus on photocatalytic nanostructures, heterojunctions and hybrid composites.

Keywords: hydrogen production; water splitting; photocatalytic nanostructures; organic–inorganic hybrid composites; sunlight activation; photocatalytic efficiency

check for updates

Academic Editor: Davide Papurello

Received: 30 April 2025
Revised: 29 May 2025
Accepted: 5 June 2025
Published: 7 June 2025

Citation: Bratovčić, A.; Tomašić, V. Hydrogen Production Through Newly Developed Photocatalytic Nanostructures and Composite Materials. *Processes* **2025**, *13*, 1813. https://doi.org/10.3390/pr13061813

Copyright: © 2025 by the authors. Licensee MDPI, Basel, Switzerland. This article is an open access article distributed under the terms and conditions of the Creative Commons Attribution (CC BY) license (https://creativecommons.org/licenses/by/4.0/).

1. Introduction

Photocatalytic hydrogen (H_2) evolution through water splitting represents a promising solution to address the global energy crisis and environmental pollution challenges. Given the distribution of solar energy (UV: 5%, visible: 43%, and infrared: 52%), the efficient harnessing of visible and near-infrared (NIR) light is essential for the development of highly efficient photocatalysts. Over the past few decades, numerous strategies have been used to enhance the light absorption capabilities of photocatalysts. These include modifying the band structure by introducing heteroatoms or defects and integrating semiconductors with other visible light-absorbing materials as a promising approach [1].

Solar energy is considered a highly promising energy source due to its cleanliness, safety, and non-reliance on transportation. Unlike fossil fuels, H_2, as one of the cleanest energy sources, offers distinct advantages such as harmless combustion (without NOx emissions), high energy density, superior conversion efficiency, and renewability. The production of sustainable H_2 energy by utilizing abundant solar energy is widely regarded as the ideal solution to address the global energy crisis and environmental challenges. In this context, photocatalytic technology using semiconductors for solar-driven H_2 production has garnered significant interest [2]. Photocatalytic H_2 production is a promising method to address the energy crisis caused by burning fossil fuels. The development of highly efficient heterojunctions for photocatalytic H_2 production is crucial for the realization of such ambitious goals and commercial application. Photocatalytic H_2 evolution from water under visible light and photocatalytic reduction of CO_2 with H_2O to form hydrocarbons (e.g., methane, methanol, ethanol, etc.) are two critical processes for the use of abundant solar energy that offer significant potential for renewable energy generation and addressing environmental challenges. Various technologies for H_2 production have been developed, mainly including thermal, biological, thermochemical and (photo)electrolytic processes. However, these technologies mostly rely on the utilization of carbon feedstocks (e.g., fossil fuels, biomass, waste) or water as an H_2 source, usually require operation at high pressures and temperatures, and are generally expensive (depending on the cost of feedstocks and related energy costs). For this reason, photoassisted processes that use solar irradiation and water, or potentially renewable feedstocks, are becoming increasingly attractive in the scientific community.

Semiconductor–metal heterostructures, particularly those involving various inorganic semiconductors coupled with platinum (Pt), are widely used for the conversion of solar energy into chemical energy. However, due to the scarcity and high cost of Pt, the development of non-Pt alternatives and efficient assembly strategies is essential. The conversion of sustainable solar energy into clean, cost-effective, and carbon-free H_2 through the use of highly efficient metal-free photocatalysts represents a promising and critical research endeavor [3]. Semiconductor photocatalysts have emerged as promising materials for photocatalytic H_2 evolution due to their ability to efficiently generate electron–hole pairs (e^--h^+) under light irradiation, thereby facilitating reduction reactions. A wide range of semiconductor photocatalysts, including transition-metal oxides, nitrides, and sulfides, have been used for photocatalytic H_2 evolution.

Photocatalytic water splitting, driven by solar energy utilizing the well-known TiO_2 P25 as a benchmark photocatalyst, has gained considerable attention as an environmentally friendly approach and a viable alternative to conventional H_2 production methods. However, TiO_2 P25 exhibits significant limitations, including rapid charge carrier recombination and a narrow light absorption range related to its wide bandgap of approximately 3.2 eV. Recent studies have focused on overcoming these limitations through the development of "new-generation" TiO_2-based materials, using various strategies of TiO_2 modifications, such as morphology control (nanorods, nanowires, nanosheets), narrowing the bandgap energy via bandgap engineering using doping with elements such as N, C and S, formation of homojunctions (inter-phase junctions, e.g., TiO_2 anatase/rutile homojunctions [4] and heterojunctions by combining TiO_2 with noble metals like Pt and Pd or by other narrow bandgap semiconductors using novel synthesis techniques to improve overall photocatalytic performance [5,6]. Nevertheless, these modifications often encounter challenges, notably in terms of cost-effectiveness and photostability, which have limited their full-scale application across various practical domains, including photocatalytic water splitting, pollutant degradation, and solar energy harvesting via solar cells.

Cobalt monoxide (CoO) is a particularly remarkable metal oxide semiconductor due to its narrow bandgap, which allows it to absorb visible light and facilitate overall water splitting reactions. However, CoO suffers from significant deactivation during photocatalytic processes, primarily due to the aggregation of CoO nanoparticles. To address the deactivation problem associated with CoO, a semiconductor with a larger specific surface area was chosen to minimize the aggregation of nanoparticles [7].

Cadmium sulfide (CdS) has attracted considerable attention as a promising photocatalyst for H_2 evolution due to its excellent response to visible light and its well-positioned conduction band. Despite its potential, the practical application of CdS in photocatalytic water splitting is still limited. This is primarily due to the low separation efficiency of the photogenerated electron–hole pairs and the problem of photocorrosion, which leads to the release of toxic Cd^{2+} ions and subsequent environmental pollution [8]. These challenges can be addressed by optimizing the band energy levels, morphologies, and microcrystal structures of metal sulfide nanoparticles (NPs). In addition, the development of composite materials has proven to be an effective strategy to mitigate the recombination of the photogenerated charge carriers, which is a key factor contributing to the deactivation of photocatalysts.

Polymeric graphitic carbon nitride (g-C_3N_4, CN) has also attracted considerable attention due to its moderate bandgap, unique optical properties, and excellent photochemical stability. Graphitic carbon nitride is an n-type metal-free semiconductor, and presents excellent redox ability to generate H_2 from H_2O under visible light irradiation. However, the practical application of g-C_3N_4 is hindered by its low visible-light utilization efficiency, rapid charge recombination, and limited specific surface area. To address these limitations, several modification strategies have been developed to improve the photocatalytic performance of g-C_3N_4. These strategies include element doping [9], noble metal deposition [10], and the formation of heterojunctions with other semiconductors [11]. Among these strategies, constructing heterojunctions is considered particularly effective in promoting the separation of e^--h^+ pairs and facilitating their transfer across interfaces. In heterojunction-based systems, continuous band bending at the interface enhances visible light absorption and supports efficient charge transfer processes. These features contribute to improved photocatalytic performance by increasing the interaction between charge carriers and light absorption. Metal oxides are commonly employed as semiconductor materials in combination with g-C_3N_4 to enhance photocatalytic activity due to their ability to promote charge separation and reduce recombination [12].

The formation of heterojunctions by coupling CN with semiconductors, such as TiO_2, ZnO, or CdS, minimizes the recombination of photogenerated electron–hole pairs by facilitating the transfer of electrons from a high reduction potential in the conduction band to a lower conduction band potential. This mechanism enhances overall photocatalytic performance, making CN-based systems promising for visible-light-driven H_2 production applications [3]. Besides CN, other carbon nanostructures (CNSs) are also attractive materials for the development of nanocomposites, heterojunctions and nanohybrids applied for H_2 production due to their unique properties such as high electron conductivity, large electron storage capacity, large surface area, suitable morphology and light absorption ability.

The energy stored in H-H bonds can be harnessed through combustion in specially designed engines, but it is more commonly associated with electricity generation in fuel cells. These electrochemical devices typically feature an anode made of platinum on conductive carbon. Fuel cells can achieve relatively high efficiencies, around 30%, in converting chemical energy into electrical energy. Hydrogen can be produced from a variety of primary sources, including natural gas, naphtha, heavy oil, methanol, biomass, waste materials, and coal, typically through a reforming process. The reaction of methane with water, for exam-

ple, produces CO_2 and H_2 with a reaction enthalpy (ΔH_{298}) of 165 kJ mol^{-1} [13]. Natural gas reforming is the most important industrial method for H_2 production. This process occurs at elevated temperatures (700–1100 °C) and utilizes nickel-based catalysts. The resulting gas mixture typically contains 75–78% hydrogen (H_2), 30% carbon dioxide (CO_2), trace amounts of methane (CH_4), and 10–20 ppm of carbon monoxide (CO) [14]. A brief overview of the various methods of H_2 production and their associated challenges, such as feedstock type, conversion efficiency, and the need for the safe integration of H_2 production systems with H_2 purification and storage technologies, can be found elsewhere [15].

Despite great progress and innovations that have been achieved in recent years, there are still numerous challenges that need to be solved to enable sustainable and applicable photocatalytic hydrogen production. These include several key aspects including the following: (a) the development of advanced composite and hybrid materials using facile synthesis and cost-effective production methods; (b) the further optimization of the composition, structure and morphology of such materials, including the application of advanced characterization techniques in combination with a theoretical modeling approach based on density functional theory (DFT) to predict and explain the electrical structure of advanced materials; and (c) the development of advanced solar reaction systems for continuous operation, the optimization of reaction conditions, and the integration of photocatalytic hydrogen production systems with hydrogen storage and purification technologies. Conflicting information can be found in the literature on specific materials and synthesis methods that provide the highest efficiency, stability and durability of such materials as critical parameters for evaluating their practical viability. Therefore, this article provides a systematic review of the recent literature on photocatalytic nanostructures, heterojunctions and hybrid composites as valuable strategies to improve photocatalytic hydrogen production by enhancing light absorption, charge separation and hydrogen evolution efficiency.

2. Basics of Photocatalytic Water Splitting

Water splitting into hydrogen (H_2) and oxygen (O_2) is a thermodynamically uphill reaction, with a positive Gibbs free energy change (ΔG° = +238 kJ/mol). For efficient photocatalytic H_2 production under visible light, the semiconductor's bandgap should be between 1.23 and 3 eV [6]. The alignment of the optical bandgap with the valence band (VB) and conduction band (CB) potentials is essential for effective oxidation and reduction reactions. The VB must have a more positive potential than the O_2/H_2O oxidation (1.23 eV), and the CB must be more negative than the H^+/H_2O reduction (0 V). Common semiconductors, like TiO_2 (3.2 eV), ZnO (3.3 eV), WO_3 (2.6 eV), and Fe_2O_3 (2.1 eV), have different bandgaps [16].

In general, H_2 production by water splitting can be divided into three types: thermochemical, photobiological, and photocatalytic. Photocatalytic water splitting is the most efficient and cost-effective, using light photons without external energy input. In this process, the light excites electrons in the photocatalyst, creating electron–hole pairs. The energy gap between the VB and CB must match the light's wavelength for effective absorption. The photoelectrons reduce H^+ ions to H_2, while the holes oxidize water to oxygen. A higher surface area of the photocatalyst improves reaction efficiency by providing more active sites.

The photocatalytic water splitting (sometimes called artificial photosynthesis) can be defined as the reaction that splits H_2O into H_2 and O_2 in a 2:1 ratio using an appropriate semiconductor photocatalyst. It involves two half-reactions, as described by the relevant Equations (1)–(3):

$$O_2 + 4H^+ + 4\,e^- \rightarrow 2H_2O \text{ (water oxidation)} \quad (1)$$

$$4H^+ + 4\,e^- \rightarrow 2H_2 \text{ (water reduction)} \quad (2)$$

$$2H_2O \rightarrow 2H_2 + O_2 \text{ (water splitting)} \quad (3)$$

Different types of semiconductor materials have been investigated and applied in photoasisted H_2 production with limited efficiency. Research has shown that the main challenges in designing suitable semiconductors include efficient charge carrier separation, fast transfer of photogenerated e^--h^+ pairs and their migration to surface reactive centers, favorable placement of band edges with redox potentials of the desired reactions, and acceptable exposure of active centers as well as simple synthesis. Manzoor et al. [16] proposed a photocatalytic reaction mechanism using copper-doped nanocomposites. In their study [16], the incorporation of copper (Cu) into the ZnO lattice reduced crystal growth, decreasing crystallite size and increasing surface area, which increased photocatalytic activity. Cu doping shifted the light absorption into the visible spectrum and minimized the recombination of photogenerated e^--h^+ pairs. Cu^{+2} ions in the ZnO lattice are reduced to metallic Cu^0 by photogenerated electrons, promoting e^--h^+ separation (Equations (4) and (5)). This reduction occurs because copper has a higher reduction potential than zinc, thereby facilitating the separation of electron–hole pairs and improving photocatalytic performance. To further enhance e^--h^+ pair separation, methanol was introduced as a hole scavenger. Under light illumination, photogenerated h^+ attacked methanol, leading to the formation of formaldehyde. This formaldehyde reacts with hydroxyl radicals (OH^-) to produce formic acid (Equations (6)–(8)). The electrons in the ZnO conduction band (CB) react with Cu^{+2} ions to reduce them into metallic Cu, resulting in the formation of metallic clusters (Equations (9) and (10)). These Cu nanoparticles act as electron sinks by trapping photogenerated electrons, thereby promoting enhanced electron–hole separation. Furthermore, the presence of Cu nanoparticles shifts the Fermi level toward a more negative potential (Equations (11) and (12)). The photoelectrons migrate toward the Cu nanoparticles until the Fermi level reaches the CB of ZnO. This movement facilitates greater e^--h^+ separation on the photocatalyst's surface, attributed to the electron sink properties of Cu. As a result, the Cu nanoparticles serve as active sites that trap photogenerated e^- or transport them to H^+ ions, leading to H_2 production (Equation (13)). The results of this study show that the introduction of Cu nanoparticles into ZnO leads to higher photocatalytic H_2 production. This improvement can be attributed to accelerated charge transport, the metallic catalytic properties of Cu, and the observed red shift in optical absorption. In this study, improved photocatalytic H_2 production was observed for the Cu-doped ZnO photocatalyst compared to pure ZnO.

$$h\nu + ZnO\ (e^- + h^+) \rightarrow ZnO \quad (4)$$

$$H_2O + h^+ \rightarrow \cdot OH + H^+ \quad (5)$$

$$CH_3OH + h^+ \rightarrow \cdot CH_2OH + H^+ \quad (6)$$

$$\cdot CH_2OH + h^+ \rightarrow HCHO + H^+ \quad (7)$$

$$\cdot OH + h^+ + HCHO \rightarrow HCOOH + H^+ \quad (8)$$

$$2\ e^- + Cu^{+2} \rightarrow Cu^0 \quad (9)$$

$$ZnO - n\ (Cu^0) \rightarrow ZnO - Cu_n{}^0 \quad (10)$$

$$h\nu + ZnO - Cu_n{}^0 \rightarrow ZnO\ (e^- + h^+) - Cu_n{}^0 \quad (11)$$

$$ZnO\ (e^- + h^+) - Cu_n{}^0 \rightarrow ZnO\ (h^+) - Cu_n{}^0\ (e^-) \quad (12)$$

$$ZnO\ (h^+) - Cu_n{}^0\ (e^-) + H^+ \rightarrow ZnO\ (h^+) - Cu_n{}^0 + \tfrac{1}{2}\ H_2 \quad (13)$$

The water molecule is very stable, and its thermal dissociation is highly endothermic ($\Delta G^\circ = -237$ kJ mol^{-1}). A temperature of 2500 K is required to achieve approximately

5% dissociation at atmospheric pressure. Contrarily, if only the thermodynamics of the process are considered, the photochemical decomposition of water appears feasible by using photons with wavelengths shorter than 1100 nm (around 1.3 eV). However, this photochemical reaction requires overcoming a substantial activation energy. Consequently, dissociation becomes significant only after irradiation with wavelengths shorter than 190 nm, and, fortunately, this process does not occur under sunlight [17]. The application of photocatalysts significantly lowers the energy barrier, making the process feasible with photons from the solar spectrum. It is crucial to note that water splitting, as well as CO_2 photoreduction, is not a spontaneous reaction, but rather an endothermic process ($\Delta G > 0$), meaning it requires the input of energy to drive the formation of chemical bonds in the products. By considering only photons with the necessary energy for water molecule photodissociation, it is theoretically possible to produce approximately 2.8 mmol s^{-1} m^{-2} of H_2 (equivalent to 800 W m^{-2}) using solar radiation. However, this value represents an idealized upper limit, as activation losses during the process would inevitably decrease the overall efficiency.

3. Newly Developed Photocatalytic Nanostructures and Composite Materials

The photoactivity of a material suitable for efficient H_2 production is primarily determined by its physicochemical properties, particularly the fundamental electronic properties related to its band-edge energy positions. The following text provides an overview of the different materials that have been developed and investigated for photocatalytic H_2 production.

3.1. Carbon-Based Materials

The development of cost-effective, efficient, photostable and completely metal-free photocatalysts is crucial to advance visible-light-driven photocatalytic production. To address these needs, various carbon-based materials, including graphene and carbon nanotubes (CNTs), have been investigated extensively. However, these materials face limitations related to preparation complexity, resource availability, and scalability. In this regard, g-C_3N_4 or CN has emerged as a more promising alternative to graphene and CNTs.

CN is a nonmetallic π-conjugated polymer with a narrow bandgap of 2.7 eV and a sufficiently negative conduction band edge, rendering it a highly promising candidate for efficient water reduction to produce H_2 [18,19]. CN possesses a range of advantageous properties, including non-toxic nature, excellent photochemical stability, intrinsic basic surface functionalities, and greater natural abundance. Furthermore, CN can be synthesized through a straightforward, one-step polymerization process using inexpensive, readily available nitrogen-rich precursors, such as melamine and urea. CN also demonstrates significant potential when combined with semiconductors like TiO_2 for improved charge transfer and charge carrier separation. Recent research to improve charge separation efficiency has largely focused on the development of composites and heterojunctions. In composite materials, the expected redox potentials can be achieved by using different nanostructured materials or nanocomposites and heterojunctions through the coupling of different semiconductors.

3.2. Composite Photocatalysts and Photocatalysts Multicomponent Heterojunctions

Heterojunction refers to the interface area formed by the contact of two or more semiconductors with unequal band structure [20]. Such an approach enables the expansion of the spectrum absorption range of a single semiconductor, promotes the migration of charges generated by light on different semiconductors through close contact at their inter-

face and improves their spatial separation, thereby enhancing their functional properties and photocatalytic performance [21,22]. Conventional heterojunction composite photocatalysts, which consist of two semiconductors with different properties (semiconductor I (PS I) and semiconductor II (PS II)), can be classified into several types based on their band alignment at the interface and charge transfer mechanism: type I, type II, type III, and S-scheme (Figure 1). Each type of heterojunction has its advantages and limitations, and the proper choice of heterojunction is very important for their practical application. An excellent overview of recent advances in semiconductor heterojunctions, including representative literature on different heterojunctions and their application, is provided by Balapure et al. [23].

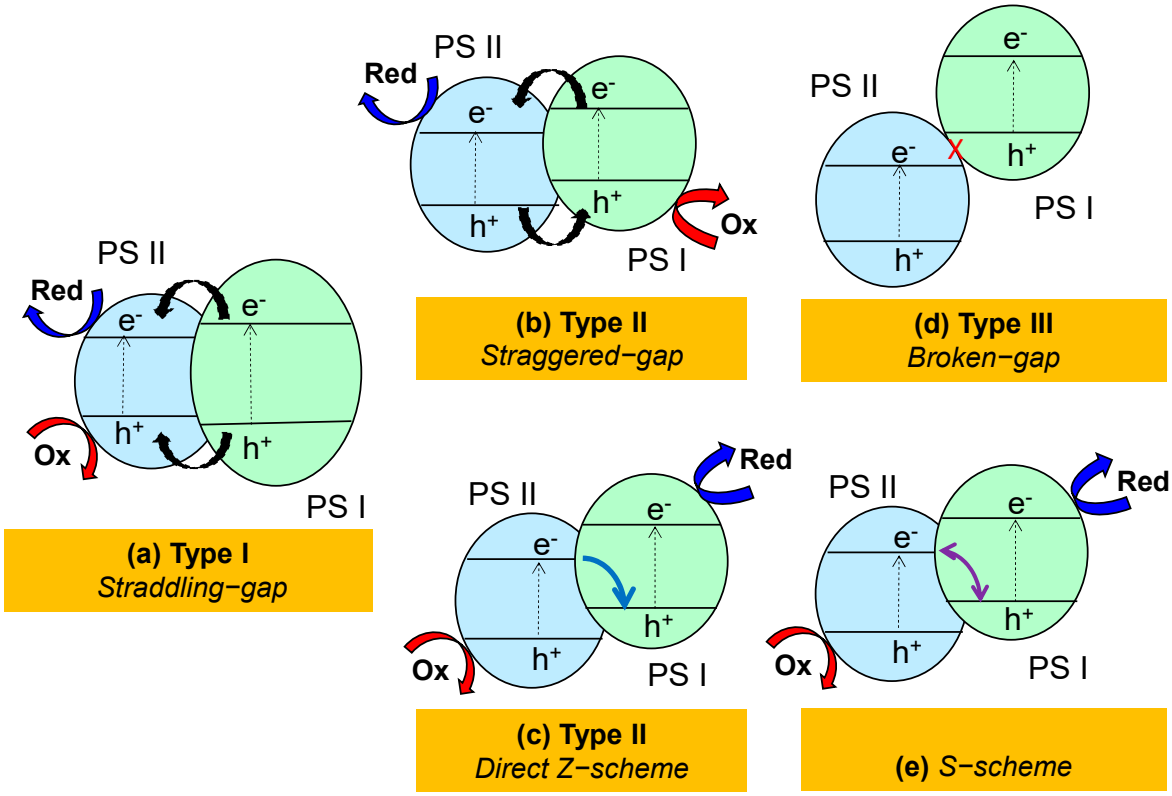


Figure 1. Different types of semiconductor heterojunctions: (**a**) type I (straddling-gap), (**b**) type II (staggered-gap), (**c**) type II (direct Z-Scheme), (**d**) type III (broken-gap), and (**e**) S-scheme.

In type I heterojunctions (straddling-gap) (Figure 1a), PC II has a narrower bandgap compared to PC I. Because PC I has a more negative CB and a more positive VB, electrons and holes move from PC I to PC II. A type I heterojunction, therefore, does not enhance charge carrier separation since all the charge accumulation occurs in one of the components and, in theory, does not improve photocatalytic activity. However, due to the abundance of wide bandgap semiconductors and the constraints on VB and CB positions, type I heterojunctions are commonly formed when composite materials consist of a narrow bandgap semiconductor and a wide bandgap semiconductor. Despite these limitations, it has been shown that the right choice of materials in type I heterojunction systems exhibits better behavior than the individual components. In type II heterojunctions (staggered-gap) (Figure 1b), the CB position of PC I is more negative than that of PC II, while PC II has a more positive VB position. As a result, electrons and holes move in opposite directions, which enhances charge carrier separation, reduces recombination, increases charge carrier lifetimes, and ultimately improves photocatalytic activity. Therefore, the type II heterojunction is more effective than the type I counterpart. Most of the composite

photocatalysts discussed in the literature, such as TiO_2/g-C_3N_4 [24], g-C_3N_4–WO_3 [25], g-C_3N_4–$BiPO_4$ [26], etc., are examples of type II heterojunctions. In type III heterojunctions (Figure 1d), the charge carrier transfer occurs similarly to type II semiconductors, but the band positions are more widely offset. Due to this significant band alignment, these systems are also referred to as broken-gap configurations, where the charge migration route is not feasible.

Photocatalysts composed of two-dimensional (2D) materials are particularly intriguing because of their unique electrical and optical properties. Type II heterojunctions based on 2D materials have been both theoretically and experimentally explored as efficient photocatalysts. While type II heterojunctions can effectively separate photoinduced charge carriers, *p*–*n* heterojunctions, based on the combination of *p*-type semiconductors (e.g., AgBr, CoO, Cu_2O, NiO) and *n*-type semiconductors (e.g., ZnO, TiO_2, CdS, g-C_3N_4), can facilitate even faster charge separation by leveraging internal electric fields [27]. There are also Z-scheme semiconductor heterojunctions with the same band configuration as type II heterostructures, which follow a different charge carrier recombination mechanism [28] (Figure 1c). Z-schemes utilize two distinct semiconductors along with a reversible donor/acceptor pair, commonly referred to as a shuttle redox mediator [28]. A Z-scheme heterojunction system is created between two semiconductors due to the small distance between the CB of one semiconductor and the VB of the other. In this arrangement, the electron in the CB of one semiconductor quickly recombines with the holes in the VB of the other semiconductor. As a result, the excited electrons in the CB of one semiconductor drive strong reduction reactions, while the holes in the VB of the other semiconductor facilitate efficient oxidation reactions [29].

Anatase titanium dioxide (TiO_2) nanosheets are intentionally designed as the *n*-type semiconductor and combined with nickel oxide (NiO) nanoparticles, which act as the *p*-type semiconductor, leading to the creation of a *p*–*n* heterojunction structure. The shortened charge transfer distance and the spontaneous formation of this *p*–*n* heterojunction enhance the photocatalyst's ability to efficiently separate photogenerated electrons and holes in space [30].

This system is inspired by the process of natural photosynthesis in green plants, where photosystems I and II absorb photons with wavelengths of 700 nm and 680 nm, respectively. In contrast to heterojunctions, the semiconductors in this system are typically not in direct contact but are electronically coupled through the redox mediator. This arrangement allows for the combination of semiconductors that are capable of only one of the two reactions—either water reduction or oxidation—due to their band potentials. For instance, WO_3, which cannot reduce H^+, can produce O_2 from an aqueous solution containing suitable electron acceptors under visible light. This makes WO_3 an effective component for O_2 evolution in Z-scheme water splitting [31]. The redox mediator also plays a crucial role in the Z-scheme water-splitting system by facilitating the transfer of electrons from the O_2 evolution photocatalyst to the H_2 evolution catalyst. As a result, the direction of charge carrier flow in Z-schemes is the opposite of that in the previously described heterojunctions involving two semiconductors [32]. However, conventional Z-scheme photocatalysts have several limitations. Notable issues include light absorption interference caused by the redox mediator, slow charge carrier transfer rates constrained by ion pair diffusion, and, as previously mentioned, pH sensitivity. Additionally, redox mediators are often prone to instability and deactivation, leading to a reduction in reaction rates. Furthermore, the photogenerated electrons in the CB of PS I and the holes in the VB of PS II, which possess strong redox abilities, can also be consumed by the redox mediator. This is referred to as a backward reaction, which negatively affects the photocatalytic process.

The close interaction between the mediator and both semiconductors promotes efficient interfacial charge carrier transfer. Commonly used solid-state electron mediators include noble metal shells/nanoparticles (such as Au, Ag, Cu, Pt) as well as graphene and carbon nanotubes. When the two semiconductors are irradiated with light, the photogenerated electrons in the CB of PS II can recombine with the photogenerated holes in the VB of PS I, facilitated by the electron mediator. This process occurs due to the low contact resistance between the mediator and both semiconductors. Upon light irradiation, the photogenerated electrons in the CB of PS II can recombine with the photogenerated holes in the VB of PS I, a process assisted by the electron mediator. This occurs due to the low contact resistance between the mediator and both semiconductors, facilitating efficient charge transfer. In contrast to the traditional Z-scheme system, backward reactions at direct Z-scheme are significantly suppressed due to the absence of redox mediators. Additionally, the shielding effect caused by redox mediators or charge carrier mediators is minimized. Similar to the all-solid-state Z-scheme, both semiconductors in direct contact are excited by light irradiation. The photogenerated electrons in the CB of PS II can recombine with the holes in the VB of PS I. As a result, the photogenerated electrons in the CB of PS I and the holes in the VB of PS II remain spatially separated, preserving their strong redox potential [33]. A key requirement for the Z-scheme charge transfer mode is a work function difference between the two semiconductors. PS I must have higher CB and VB positions, as well as a smaller work function (higher Fermi level) than PS II. When the two semiconductors come into contact, electron transfer from PS I to PS II occurs due to Fermi level equilibration (similar to the *n*–*n* type direct Z-scheme shown in Figure 2).

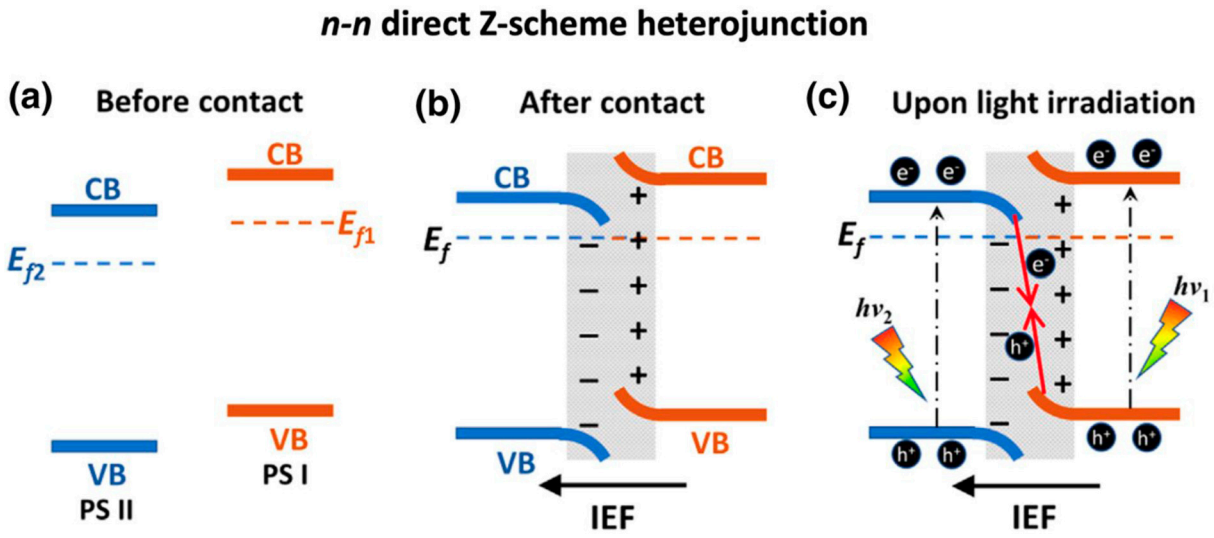


Figure 2. Schematic of *n*–*n* type heterojunction: (**a**) before contact, (**b**) after contact, and (**c**) formation of direct Z-scheme charge transfer upon light irradiation. E_f and IEF stand for Fermi level and internal electric field, respectively. Reprinted with permission from [34]. Copyright (2021), Elsevier.

Thus, the PS I side becomes positively charged, while the PS II side is negatively charged. This results in the formation of an internal electric field (IEF) and band bending. The energy band edges of PS II bend downward due to the accumulation of electrons, while the energy band edges of PS I bend upward due to a decreased electron density [35]. The IEF, along with the additional potential barrier created by band bending and Coulomb repulsion, impedes the transfer of photogenerated electrons from the CB of PS I to the CB of PS II. This also applies to the photogenerated holes in the VB of PS II.

A similar process takes place in the formation of a *p*–*n* type direct Z-scheme. However, when the Fermi level of a *p*-type semiconductor (*p*-PS) is lower than that of an *n*-type

semiconductor (*n*-PS), a type II heterojunction is formed. At their interface, the energy band edges bend in an inverted manner (Figure 3). As a result, under light irradiation, photogenerated electrons move from the *p*-PS to the *n*-PS, while holes move in the opposite direction, driven by the internal electric field (IEF). While the Fermi level alignment is relatively straightforward for *n*–*n* type heterojunctions (Figure 2), it is more challenging to achieve in *p*–*n* heterojunctions due to the significant band offset (Figure 3). Consequently, most direct Z-scheme systems are constructed with *n*–*n* heterojunctions, and only a few p–n type direct Z-scheme systems, such as $CuInS_2/WO_3$, $CuAl_2O_4/Bi_2WO_6$, and Cu_2O/TiO_2 can be found in the literature [34].

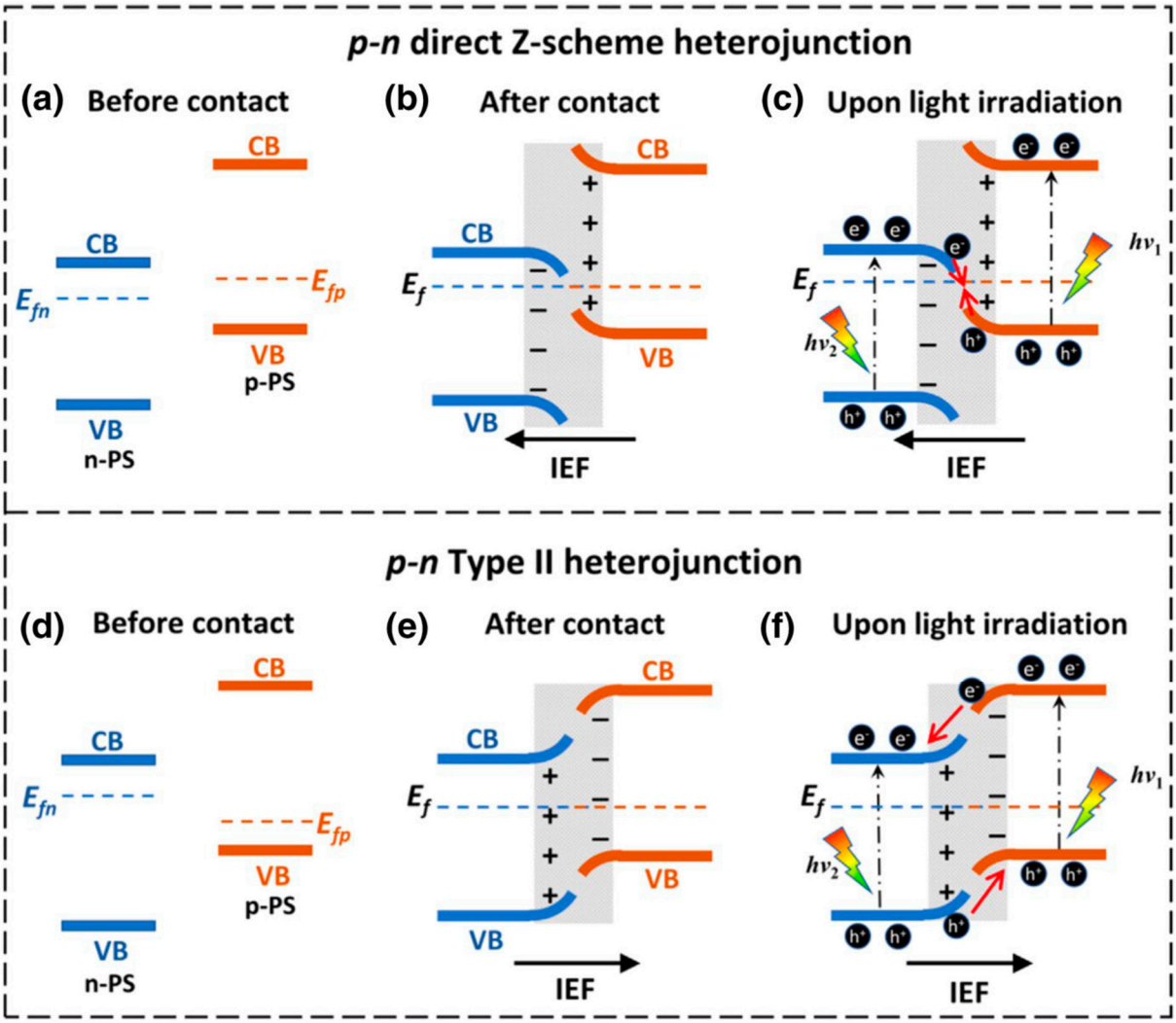


Figure 3. Schematic of (**a**–**c**) *p*–*n* direct Z-scheme heterojunction and (**d**–**f**) *p*–*n* type II heterojunction. Reprinted with permission from [34]. Copyright (2021), Elsevier.

As already mentioned, the band alignment in Z-scheme heterojunctions is similar to that of type II heterojunctions, but the mechanisms of charge transfer differ. Direct Z-schemes can also be constructed using a combination of three semiconductors. These photocatalysts are commonly referred to as "dual Z-schemes" or "ternary Z-schemes". To better understand the specific charge transfer process, multiple techniques can be employed, including self-confirmation through photocatalytic reaction products and radical species, selective photodeposition of noble metals, in situ irradiated X-ray photoelectron spectroscopy (XPS) analysis, surface photovoltage (SPV) measurements, and time-resolved diffuse reflectance (TDR) spectroscopy [33]. In some cases, the reduced photocorrosion

effects can also serve as an indication of a Z-scheme mechanism, as observed in composite materials containing CdS [36]. Despite some limitations, Z-type heterojunctions are included in the list of suitable candidates for industrial applications [22,28,37]. Representative examples of materials belonging to the Z-scheme type photocatalysts active for hydrogen generation are ZnS/ZnO nanosheets, $CoTiO_3/Cu/TiO_2$, $CoTiO_3/Zn_{0.5}Cd_{0.5}S$, g-$C_3N_4/MoO_{3-x}$ [23].

Finally, the term S-scheme (or step scheme) was also introduced, which is often used interchangeably with direct Z-schemes (Figure 1e). This type of composite catalyst has been intensively studied for the photocatalytic production of hydrogen and H_2O_2, the photocatalytic reduction of CO_2, bacteria disinfection, and the photocatalytic degradation of organic pollutants [37]. An S-scheme heterojunction consists of a reduction semiconductor and an oxidation semiconductor. For the design of S-scheme heterojunctions, *p*-type and *n*-type semiconductors can be used, provided that the CB position and Fermi level of the reduction semiconductor are higher than those of the oxidation semiconductor. This heterostructure provides strong photogenerated charge carriers of holes and electrons in the VB of the oxidation photocatalyst and CB of the reduction photocatalyst, sacrificing those that are useless in recombination. The aforementioned strong charge carriers can thus lead to a strong redox capability, together with efficient charge carrier separation and an extended lifetime of the electron–hole pair. Some of the representative examples of materials belonging to the S-scheme are SnS_2/RGO/g-C_3N_4, TiO_2-X/BiOI, Co_9S_8/In_2O_3, $ZnIn_2S_4$-$NiSe_2/Ti_3C_2$ [23]. Despite great progress in the development of S-scheme heterojunctions, there are still major challenges, such as the discovery of new semiconductors with targeted band structures as oxidation semiconductors and reduction semiconductors through machine learning, new strategies for the fabrication of specific materials with unique physicochemical properties, combination of S-scheme heterojunctions with other modification strategies (e.g., heteroatom doping, co-catalyst loading, defect and morphology engineering, etc.).

3.3. Metal–Organic Frameworks (MOFs)

Metal–organic frameworks (MOFs) are one (0)-, two (2D)-, or three-dimensional (3D) coordination networks composed of metal ions or clusters connected by organic linker molecules. MOFs have garnered increasing interest in the development of direct Z-scheme photocatalysts. The advantages of MOFs, such as tunable composition and light-harvesting properties, high surface area, and controllable pore size, make them highly attractive for photocatalytic applications [38]. While the visible light photocatalytic performance of pure MOFs is generally limited, significant improvements have been observed when they are used in direct Z-scheme systems. MOFs are a novel class of porous solid materials, renowned for their tunable structure and functionality, as well as their high specific surface area, which facilitates rapid transfer of photogenerated charges to the MOF surface for redox reactions, thus reducing the recombination of photogenerated electrons and holes during photocatalysis. TiATA, a well-known MOF, demonstrates excellent chemical stability and photocatalytic performance under visible light. The coupling of MOFs and carbon nitride is a feasible strategy in the field of H_2 evolution [39].

3.4. Covalent Organic Frameworks (COFs)

Covalent organic frameworks (COFs) are crystalline covalent polymers with a large surface area. These porous materials, which offer tunable topology and functionalities, have attracted significant interest in the field of photocatalysis [40]. The moderate bandgap and the presence of extended π-conjugated electronic networks allow for visible-light responsiveness and provide opportunities for bandgap engineering. As a result, COFs and COF-linked hybrid materials are employed as photocatalysts for H_2 production. Due to the

stability of the covalent bonds compared to the coordinate bonds found in MOFs, COFs are known to exhibit high stability in various solvents, even under harsh acidic, basic, oxidative, or reductive conditions. However, most reported photocatalytic COFs are based on imine, hydrazone, or azine linkages, which are considered unstable for prolonged photocatalysis in aqueous environments. COFs are especially excellent platforms for photocatalysis due to their distinctive pore-like architecture and the robust covalent interactions within the frameworks. Nevertheless, obstacles remain in enhancing photocatalytic efficiency. It has been shown that merging the benefits of inorganic semiconductors (different microstructures and manageable bandgap) and organic frameworks to create organic–inorganic hybrid composite photocatalysts (heterojunctions) may enhanced the photocatalytic performance of materials [41].

Another approach to enhance photocatalytic activity is the integration of surface plasmon resonance (SPR) into direct Z-schemes. SPR refers to the collective oscillation of electrons that resonate with the oscillating electric field of incident light. Resonances in the visible or near-infrared range can significantly improve the light absorption capacity of the photocatalytic system. In addition, SPR-induced hot plasmon electrons or SPR-enhanced localized electromagnetic fields can facilitate charge separation at the interfaces between the SPR material and the semiconductor [42].

3.5. Hybrid Materials

Photocatalytic H_2 production can effectively tackle energy shortages and environmental challenges. The successful integration of different semiconductor materials can inhibit exciton recombination, rendering it a very efficient approach to boost photocatalytic activity. Although composites share some similarities with hybrid materials, it is important to emphasize that composites cover a broader range of dimensions of mixed components, while hybrid materials usually refer to the constituents at the nanometer or molecular level [43]. Various hybrid materials are used in the context of photocatalytic H_2 production, such as the combination of polymer materials with metal oxide photocatalysts.

3.5.1. Two-Component Composites Based on Graphitic Carbon Nitride (g-C_3N_4) and Organic–Inorganic Hybrid Composites

In Table 1 are listed different organic–inorganic hybrid photocatalytic composites for H_2 production.

The PCN/molybdenite nanocomposites (PCN/Mo-x) were constructed from low-cost molybdenite mineral as an effective co-catalyst, and polymeric carbon nitride (PCN) through Na_2SO_4-assisted ball milling [2].

Wadhai et al. [3] investigated the incorporation of phosphorus doping into graphitic carbon nitride (CN) and its subsequent coupling with commercial TiO_2 (P25) to improve photocatalytic H_2 evolution. The phosphorus-doped graphitic carbon nitride (PCN) was synthesized by a simple calcination method using 1-hydroxyethane-1,1-diphosphonic acid (HEDP) as the phosphorus source. It was found that phosphorus doping (anion doping) in CN subsequently coupled with P25 improved its electrical conductivity, optoelectronic and textural properties, leading to a significant improvement in photocatalytic performance. A comparative analysis between CN, PCN and their respective composites with P25 was performed. The optimized PCN-P25 composite showed a significant increase in H_2 production compared to P25, CN, PCN and other CN/PCN-based composites [3].

Ying et al. 2021 prepared CoO quantum dots (QDs) within hollow-sphere g-C_3N_4 (SCNO) [7]. This approach successfully reduced the particle size of CoO QDs and ensured their high dispersion within the SCNO matrix. These effects facilitated the rapid separation and transfer of photogenerated charge carriers, thereby enhancing the photocatalytic H_2 evolution performance. The incorporation of volatile gases during the process effectively

inhibited the aggregation of CoO QDs, providing optimal conditions for their uniform distribution [7].

In the case of bare g-C_3N_4 (CN), significant charge recombination and intense fluorescence occur, which have a negative effect on the photocatalytic processes. In their study, Lu et al. (2024) [44] bent g-C_3N_4 into nanotubes and then fused them with black phosphorus quantum dots (BPQDs). The BPQDs functionalized tubular CN (BPTCN) demonstrates a consistent and elevated photocatalytic H_2 production rate of 507.51 μmol h^{-1} g^{-1} under visible light, which is four times greater than that of pure TCN. The apparent quantum yield of BPTCN at 420 nm attains 2.58%. The remarkable photocatalytic performance of the BPTCN is due to the reduced recombination of electron–hole pairs and the enhanced carrier transport efficiency, both of which are facilitated by the 1D tubular design and the band alignment of the BPTCN heterojunction.

Augustin et al. (2024) [45] prepared an organic–inorganic hybrid composite from carbon nitride (C_3N_5) conjugated polymer enclosed with a ceric oxide (CeO_2) metal oxide photocatalyst. The encapsulation of the polymer with CeO_2 nanoparticles led to outstanding performance in H_2 production, demonstrating enhanced visible light absorption and a remarkable increase in charge transfer efficiency. This is due to the increased charge transfer and diminished recombination in the composite. Furthermore, the generation of holes by light resulted in a significant reduction in the exciton recombination rate and a simultaneous increase in the photocatalytic H_2 production rate. Remarkably, the measured H_2 evolution for the C_3N_5 composites doped with 10 wt% CeO_2 is 1256 μmol g^{-1} h^{-1}, while for C_3N_5 alone, it is 125 μmol g^{-1} h^{-1}. Interestingly, the proposed system represents an innovative approach to H_2 evolution by photocatalysis using CeO_2/C_3N_5 composites [40]. The extended light absorption and inhibited charge recombination are essential for photocatalytic materials based on g-C_3N_4.

Huang et al. (2022) [46] synthesized nonstoichiometric molybdenum oxide (MoO_{3-x}) nanorods with oxygen vacancies using a small quantity of oleylamine, and they produced the Z-scheme two-dimensional (2D)/one-dimensional (1D) g-C_3N_4/MoO_{3-x} composites via a simple electrostatic assembly technique. The blue MoO_{3-x} nanorods with oxygen vacancies are evenly distributed on the g-C_3N_4 nanosheets. The g-C_3N_4/MoO_{3-x} composite materials show significant absorption in the visible and near-infrared light ranges, along with enhanced charge separation efficiency via the Z-scheme charge transfer mechanism. The g-C_3N_4/MoO_{3-x} composite exhibits a notably enhanced photocatalytic H_2 production efficiency and excellent cycling stability when compared to sonicated g-C_3N_4 nanosheets. The g-C_3N_4/MoO_{3-x} composite with a mass percent of 27.5% achieves the highest H_2 generation activity of 209.2 μmol h^{-1} under solar light and an apparent quantum efficiency of 4.4% when irradiated at 365 nm, which is 2.63 times greater than g-C_3N_4. The weight ratios along with the presence of oxygen vacancies in the smaller MoO_{3-x} nanorods exhibit a considerable impact on photocatalytic H_2 efficiency. Additionally, successful overall water splitting via photocatalysis can be accomplished with the H_2 and O_2 generation rates of 0.755 and 0.368 μmol h^{-1} using the g-C_3N_4/MoO_{3-x} composite. The innovative g-C_3N_4/MoO_{3-x} composite is expected to have significant potential for photocatalytic applications.

Table 1. Recently developed organic–inorganic hybrid photocatalytic composites for photocatalytic H_2 production.

Photocatalytic Composites, Organic–Inorganic Hybride	Advantage	H_2 Production	Ref.
NaYF4:Yb,Er/CdS-380	λ > 400 nm, λ > 600 nm, 300 W Xe lamp Critical role of structural and interfacial engineering in enhancing photocatalytic performance Na_2S/Na_2SO_3 as sacrificial agents NaYF4:Yb,Er enhances photocatalytic activity by converting (NIR) light into (VIS) light, which can then excite the CdS photocatalyst. The role of upconversion processes in promoting photocatalytic performance.	2.539 mmol h^{-1} g^{-1} 0.019 mmol h^{-1} g^{-1}	[1]
Polymeric carbon nitride (PCN)/molybdenite nanocomposites (PCN/Mo-x)	Molybdenite replaced the Pt co-catalyst, improve the separation efficiency of photoinduced e^- and h^+, enhance light absorption, 0.75 M triethanolamine (TEOA) aqueous solution, with TEOA acting as a sacrificial agent, λ > 420 nm, 300 W Xe lamp.	bulk-PCN/Pt-0.067 mmol g^{-1} h^{-1} and PCN/Pt-0.08 mmol g^{-1} h^{-1} PCN/Mo-1, 2, and 3 0.016, 0.027, and 0.019 mmol g^{-1} h^{-1}	[2]
Phosphorus-doped graphitic carbon nitride (PCN) 1-Hydroxyethane-1,1-diphosphonic acid (HEDP) as the phosphorus source and carbon nitride (CN)	1000 W xenon lamp, 10% methanol solution	3.0CN–P25 composite–0.92 mmol/g CN alone (0.041 mmol/g) P25 alone (0.099 mmol/g) 2.0PCN–P25 composite–2.531 mmol/g	[3]
CoO quantum dots within hollow-sphere g-C_3N_4 (SCNO)	λ > 420 nm, 300 W Xe lamp, water and triethanolamine (TEOA)-as the sacrificial agent, in a volume ratio of 9:1	SCNO/CoO (0.2)–11.495 mmol H_2 h^{-1} g^{-1}	[7]
CdS@NC composites; CdS nanoparticles, were simultaneously deposited on nitrogen-doped carbon (NC) CdS@NC-500-4	λ ≥ 420 nm, Na_2S/Na_2SO_3 as sacrificial agents, Assembly of Cd^{2+} and MO anions into a crystalline phase is essential for optimizing photocatalytic performance.	7.428 mmol h^{-1} g^{-1}	[8]

Table 1. *Cont.*

Photocatalytic Composites, Organic–Inorganic Hybride	Advantage	H_2 Production	Ref.
Bent g-C_3N_4 into nanotubes and subsequently merged it with black phosphorus quantum dots (BPQDs)	λ = 420 nm	0.50751 mmol h^{-1} g^{-1}	[44]
C_3N_5 conjugated polymer-ceric oxide (CeO_2) (10 wt% CeO_2)		1.256 mmol g^{-1} h^{-1}	[45]
Z-scheme two-dimensional (2D)/one-dimensional (1D) g-C_3N_4/MoO_{3-x} composites MoO_{3-x} nanorods on the g-C_3N_4 nanosheets	365 nm	0.2092 mmol h^{-1}	[46]

A novel biochar/$ZnFe_2O_4$ (BZF) composite has been developed to enhance the efficiency of visible-light-driven H_2 evolution through a straightforward microwave hydrothermal synthesis method [47]. The results showed that different biochar/$ZnFe_2O_4$ (BZF) composite ratios exhibited superior photocatalytic H_2 evolution performance compared to pure $ZnFe_2O_4$. Notably, the BZF composite with a 5:1 mass ratio (BZF-5) achieved the highest H_2 evolution rate, approximately six times greater than that of pure $ZnFe_2O_4$. The biochar component serves as an effective electron mediator, promoting the separation of electron–hole pairs and thereby enhancing the photocatalytic H_2 evolution rate. Additionally, the synergistic effects of Eosin Y, the photocatalyst, and triethanolamine (TEOA) contributed to the improved photocatalytic performance. Three consecutive cycles of photocatalytic H_2 evolution using the BZF-5 sample confirmed its excellent stability and reusable performance.

Major Achievements in the Development of Organic–Inorganic Hybrid Photocatalytic Composites for Photocatalytic H_2 Production

The previous studies investigated various strategies for enhancing photocatalytic H_2 evolution through material modifications and composites. Wadhai et al. [3] demonstrated that phosphorus doping in graphitic carbon nitride (PCN) significantly improved its electrical conductivity and photocatalytic performance when coupled with TiO_2 (P25), leading to enhanced H_2 production. Ying et al. (2021) [7] successfully incorporated CoO quantum dots (QDs) within hollow-sphere g-C_3N_4, which improved the dispersion and charge carrier separation, thus enhancing photocatalytic efficiency. Similarly, Lu et al. (2024) [44] achieved four times greater H_2 production by fusing black phosphorus quantum dots with tubular g-C_3N_4, facilitating improved charge transport and reduced electron–hole recombination. Augustin et al. (2024) [45] synthesized an organic–inorganic hybrid composite with CeO_2 and C_3N_5, showing outstanding performance with a remarkable increase in H_2 evolution due to enhanced charge transfer and light absorption. Huang et al. (2022) [46] fabricated a g-C_3N_4/MoO_3-x composite with oxygen vacancies, significantly enhancing photocatalytic efficiency and stability due to better charge separation and visible light absorption. The integration of MoO_3-x into g-C_3N_4 also led to increased overall water splitting, demonstrating the composite's potential in photocatalytic applications. Additionally, a novel

biochar/$ZnFe_2O_4$ composite was developed with microwave hydrothermal synthesis, achieving six times higher H_2 production than pure $ZnFe_2O_4$ by promoting electron–hole separation. The biochar acted as an electron mediator, enhancing charge separation, and improving photocatalytic H_2 evolution. These studies underscore the importance of material design, including doping, composite formation, and structural optimization, in achieving efficient photocatalytic H_2 production under visible light. The combined effects of material modifications, such as increased charge separation, improved stability, and extended light absorption, are crucial for advancing photocatalytic technologies for renewable energy generation.

3.5.2. Two-Component and Three-Component Z-Type Heterojunctions

In Table 2 are listed recently developed Z-Type heterojunction photocatalytic composites for photocatalytic H_2 production. Widely used catalysts, such as sulfides, encounter significant issues with photogenerated carrier recombination and with photocorrosion. To address this problem, Xie et al. (2025) [48] recently constructed a Z-type heterojunction $Pt/Zn_{0.2}Cd_{0.8}S/Cs_3PW_{12}O_{40}$ and presented a new approach to reduce photocorrosion of sulfides and utilize polyoxometalates in photocatalytic H_2 generation. Polyoxometalates, such as $Cs_3PW_{12}O_{40}$, which exhibit a reversible photochromic effect, and $Zn_{0.2}Cd_{0.8}S$, which is photocorrosive, enhance the separation of photogenerated charge carriers while synergistically interacting with the distinct photochromic properties of $Cs_3PW_{12}O_{40}$ to reduce photocorrosive effects. Furthermore, by incorporating the co-catalyst Pt to create a Schottky barrier that enhances the separation of photogenerated charge carriers, the $Pt/Zn_{0.2}Cd_{0.8}S/Cs_3PW_{12}O_{40}$ Z-type heterojunction ternary composites were effectively designed and used for photocatalytic H_2 generation for the first time. The optimal heterojunction composite exhibited a photocatalytic H_2 precipitation rate of 10.4 mmol g^{-1} h^{-1}, and its apparent quantum efficiency at a wavelength of 420 nm was able to achieve 8.15%.

Table 2. Recently developed Z-type heterojunction photocatalytic composites for photocatalytic H_2 production.

Photocatalytic Composites Z-Type Heterojunction	Advantage	H_2 Production	Ref.
g-C_3N_4@TiATA composites Ti-MOFs (TiATA) were coupled with metal-free graphitic carbon nitride (g-C_3N_4)	300 W Xenon lamp, extends the light absorption range of g-C_3N_4@TiATA to 490 nm, significantly accelerates charge migration	0.2658 mmol h^{-1}	[39]
Organic–inorganic hybrid Covalent organic frameworks (COFs) BDA-THTA-30		9.69184 mmol g^{-1} h^{-1}	[41]
Z-type heterojunction $Pt/Zn_{0.2}Cd_{0.8}S/Cs_3PW_{12}O_{40}$	Reducing the photocorrosion of sulfides, λ = 420 nm	10.4 mmol g^{-1} h^{-1}	[48]
$CdS/ZnIn_2S_4$, $ZnIn_2S_4$ 0.3wt%	LED light	5.80 mmol g^{-1}	[49]
Z-scheme 2D-0D $MnPS_3$-$Cs_4W_{11}O_{35}$ composite; $Cs_4W_{11}O_{35}$ (10.9 wt%)		0.0996 mmol g^{-1} h^{-1}	[50]

Table 2. *Cont.*

Photocatalytic Composites Z-Type Heterojunction	Advantage	H_2 Production	Ref.
Heterojunction B/$CoMoO_4$	Incorporation of nonmetallic atoms like B enhances the specific surface area, increases the bandgap	7.460 mmol g^{-1} h^{-1}	[51]
CuS/$NaNbO_3$ p–n heterojunction CuS nanoparticles and $NaNbO_3$ nanorods		1.603 mmol g^{-1} h^{-1}	[52]
2.5% $Co_{1.29}Ni_{1.71}O_4/TiO_2$ hybrid heterojunction	365 nm LED	1.685 mmol g^{-1} h^{-1}	[53]
C@$Zn_xCd_{1-x}S/Co_3O_4$ (30%)	10 vol% lactic acid aqueous solution, 5 W LED lamp, p–n heterostructure between Co_3O_4 and ZCS accelerates the separation of carriers, carbon particles accelerated the e^- transfer and inhibited the recombination of e^- and h^+.	(C@ZCS/CO-30)-1.4051 mmol	[54]
5% Co_3O_4/CdS/g-C_3N_4 CdS/g-C_3N_4		30.880 mmol h^{-1} g^{-1} 4.177 mmol h^{-1} g^{-1}	[55]
NiS/WO_3/g-C_3N_4 CNWN-4	5 W LED, $\lambda \geq 420$ nm, aqueous solution of 15% TEOA-as a sacrificial hole scavenger, eosin Y (EY) and co-catalyst g-C_3N_4 Incorporation of WO_3 and NiS significantly enhanced photocatalytic activity by increasing the number of active sites and improving electron mobility.	2.9291 mmol g^{-1} h^{-1}.	[56]
MMT/g-C_3N_4/15%NiCoP composites	420 nm	12.50 mmol h^{-1} g^{-1} at pH 11 under 1.0 mmol L^{-1} of eosin Y (EY) sensitization	[57]
3D hollow-sphere structure of graphitic carbon nitride (g-C_3N_4)	300 W Xe lamp, water and triethanolamine (TEOA) at a volume ratio of 9:1, Pd nanoparticles enhancing visible light absorption, acting as e^- acceptors, are incorporated into g-C_3N_4, which increases the material's ability to trap transition e^-, boosting the number of photogenerated carriers.	Pd/SCN (10 h)–0.2679 mmol/h	[58]

Table 2. *Cont.*

Photocatalytic Composites Z-Type Heterojunction	Advantage	H_2 Production	Ref.
CdNCN-CdS heterostructure	Visible light	14.7 mmol g^{-1} h^{-1}	[59]
Nanostructure composite NdOCl/Fe_2O_3/$NdFeO_3$	Methanol as the sacrificial agent	0.01279 mmol g^{-1} h^{-1}	[60]
Nanostructure composite NdOCl/Fe_2O_3/$NdFeO_3$	Triethanolamine as the sacrificial agent	0.01899 mmol g^{-1} h^{-1}	[60]

However, the development of semiconductor-based heterojunctions at the atomic scale remains a considerable challenge. In their study, Li et al. (2021) [49] introduced innovative atomic CdS/$ZnIn_2S_4$ heterojunctions created by the in situ epitaxial growth of 2D $ZnIn_2S_4$ nanosheets on the surface of 1D defective CdS nanorods.

As a potential new photocatalyst for H_2 production, $MnPS_3$ faced reduced photocatalytic activity due to its increased electron–hole recombination rate and inadequate oxidation capacity of holes. Chen et al. (2021) [50] developed a novel Z-scheme 2D-0D $MnPS_3$-$Cs_4W_{11}O_{35}$ composite for photocatalytic H_2 evolution. The $MnPS_3$-$Cs_4W_{11}O_{35}$ composites achieve the highest H_2 evolution rate of 99.6 μmol g^{-1} h^{-1} when the $Cs_4W_{11}O_{35}$ content is 10.9% by mass, which is 2.9 times greater than that of $MnPS_3$ nanosheets alone. Moreover, the photocatalytic performance of $MnPS_3$-$Cs_4W_{11}O_{35}$ remains almost stable after four cycles. $MnPS_3$ is a non-toxic p-type direct bandgap semiconductor known for its strong visible light absorption capabilities. This unique structure makes $MnPS_3$ a promising candidate for photocatalysts, as it possesses a suitable bandgap and favorable band positions for photocatalytic water splitting. Despite these advantages, the photocatalytic H_2 evolution rate of $MnPS_3$ nanosheets remains relatively low (21.2 mmol h^{-1} g^{-1}) due to a high photoelectron–hole recombination rate and insufficient oxygen production. To enhance photocatalytic performance, it is important to exfoliate high-quality $MnPS_3$ nanosheets to create effective heterojunctions. Cesium tungstate ($Cs_4W_{11}O_{35}$) is an n-type semiconductor with a bandgap of 3.0 eV [50]. Its valence band potential is more positive than the oxidation potential of oxygen, giving it a strong ability to oxidize holes. Additionally, due to the presence of pentavalent tungsten and oxygen vacancies, cesium tungstate displays significant localized surface plasmon resonance (LSPR) absorption in the visible and near-infrared light regions, which is advantageous for improving photocatalytic reaction activity. Energy level analysis and photocatalytic mechanisms indicate that the $MnPS_3$-$Cs_4W_{11}O_{35}$ composite could significantly enhance H_2 production activity. However, $MnPS_3$ tends to oxidize during the second step of the hydrothermal process, making it difficult to load semiconductors with highly positive valence bands onto its surface using conventional chemical synthesis methods. Therefore, a gentle electrostatic assembly technique is highly desirable to uniformly immobilize $Cs_4W_{11}O_{35}$ nanoparticles on the $MnPS_3$ nanosheets, to improve charge separation efficiency and photocatalytic performance.

Li et al. (2025) [51] provided a theoretical backing for improving the photocatalytic H_2 production capability of catalysts through the incorporation of nonmetallic atoms like B or the formation of heterojunctions, presenting a viable concept for the industrial use of photocatalytic H_2 production. Since the B atom is rather electronegative, it can provide abundant electrons for H_2 generation. In this study, a composite catalyst B/CoMoO4 was prepared by the incorporation of B powder during the in situ hydrothermal synthesis of CoMoO4. Doping with nonmetallic B increases the specific surface area of the catalyst and increases the bandgap of the catalyst. Abundant reactive sites and a comparatively low electron shift resistance improve photocatalytic H_2 production. Due to the electron

exchange between nonmetal B and $CoMoO_4$ at the contact interface, the rate of electron shift is enhanced, resulting in a catalyst surface with a robust oxidation-reduction capability. The results of the photocatalytic H_2 evolution test indicate that the H_2 production rate of B/$CoMoO_4$ attains 7460 μmol g^{-1} h^{-1}, which is 4.2 times greater than that of the $CoMoO_4$ catalyst, and exhibits strong stability.

As mentioned, the p–n heterojunction is an important type of heterojunction characterized by an internal electric field due to the different properties of semiconductors. In their study, Chang et al. (2023) [52] described the creation of a new CuS/$NaNbO_3$ p–n heterojunction through the application of CuS nanoparticles onto the outer surface of $NaNbO_3$ nanorods to enhance photocatalytic H_2 generation. The best H_2 production activity was achieved at 1603 μmol g^{-1} h^{-1}, significantly surpassing that of $NaNbO_3$ (3.6 times greater) and CuS (2.7 times greater). Therefore, the presence of p–n heterojunction interactions between the two materials prevented the recombination of photogenerated charge carriers and enhanced electron transfer efficiency.

Fang et al. (2023) [53] showed that $Co_{1.29}Ni_{1.71}O_4$ serves as a promising heterojunction counterpart material and can enhance photocatalysis via distinct cross-boundary charge transfer. In this study, a new n-type TiO_2 sourced from glycerolate, featuring oxygen vacancies, was hybridized with $Co_{1.29}Ni_{1.71}O_4$ through a straightforward ultrasonication technique to achieve this goal. The optimized 2.5% $Co_{1.29}Ni_{1.71}O_4$/TiO_2 hybrid exhibited a photocatalytic H_2 production rate of 1685 μmol g^{-1} h^{-1} when exposed to 365 nm LED light, which is 26.7 times greater than that of pure TiO_2 (63 μmol g^{-1} h^{-1}). Moreover, the quantity of H_2 produced exhibited a linear rise with the prolongation of irradiation time for the 2.5% $Co_{1.29}Ni_{1.71}O_4$/TiO_2 catalyst throughout a 24-h continuous H_2 release experiment, validating its remarkable catalytic stability. Thorough characterizations showed that the $Co_{1.29}Ni_{1.71}O_4$ nanosheet was in close contact with TiO_2 nanoparticles, enhancing the specific surface area and broadening the light absorption spectrum of TiO_2.

A high-performance catalyst for H_2 production, C@$Zn_xCd_{1-x}S$/Co_3O_4, was successfully prepared by Li et al. [54] following a two-step modification process. The light absorption intensity of both C@$Zn_xCd_{1-x}S$ and C@$Zn_xCd_{1-x}S$/Co_3O_4 exhibited an increasing trend compared to that of pure $Zn_xCd_{1-x}S$. This improvement was beneficial for visible-light absorption and the utilization of the photocatalyst. Mott–Schottky analysis confirmed that the ZnxCd1-xS catalyst formed a p–n heterojunction with Co_3O_4 nanoparticles, further confirming the successful modification of C@$Zn_xCd_{1-x}S$ with Co_3O_4. The H_2 production rate of the optimized C@$Zn_xCd_{1-x}S$/Co_3O_4 (30%) catalyst reached 1405.1 μmol, which was 6.9 times higher than that of pure $Zn_xCd_{1-x}S$.

In their study, Wu et al. [55] synthesized a series of CdS-based ternary composites (Co_3O_4/CdS/g-C_3N_4) by forming a heterojunction through a simple self-assembly approach followed by a solvothermal in situ process to enable efficient photocatalytic H_2 production. The experimental findings revealed that the 5% Co_3O_4/CdS/g-C_3N_4 nanocomposite exhibited a superior photocatalytic H_2 evolution rate of 30 880 μmol h^{-1} g^{-1} under visible light illumination—approximately 17.1 times higher than that observed for pure CdS alone. This enhanced photocatalytic performance can be attributed to synergistic interactions among the constituent materials, which promote efficient separation of photoinduced charge carriers. This study highlights the promising potential of CdS-based ternary heterostructures for the further development of photocatalytic H_2 generation.

Pure g-C_3N_4 and CdS exhibit relatively low H_2 evolution rates, with values of 823 and 1806 μmol h^{-1} g^{-1}, respectively. The apparent quantum efficiency (AQE) of 5% CdS is calculated to be 3.4%. However, when g-C_3N_4 is encapsulated within CdS nanorods to form CdS/g-C_3N_4, the H_2 production rate increases to 4177 μmol h^{-1} g^{-1}. Notably, the ternary Co_3O_4/CdS/g-C_3N_4 composites showed a significant enhancement in photocat-

alytic performance, with an optimal loading amount of 5%. The 5% Co_3O_4/CdS/g-C_3N_4 composite achieved the highest photocatalytic H_2 evolution rate of 30,880 μmol h^{-1} g^{-1}, accompanied by an AQE of 30.7%. These represent approximately 17-fold and 7-fold improvements compared to pure CdS and CdS/g-C_3N_4, respectively. A comparison between 5% Co_3O_4/CdS and 5%Co_3O_4/CdS/g-C_3N_4 also indicated that the superior photocatalytic performance of the latter was due to the synergistic effects of the ternary heterojunction. Recycling experiments and consistent XRD patterns of 5% Co_3O_4/CdS/g-C_3N_4 before and after testing confirmed the composite's photochemical stability.

Zhang et al. 2020 [56] presents a novel and efficient strategy to significantly enhance the H_2 production performance of g-C_3N_4 by synthesizing a NiS/WO_3/g-C_3N_4 composite. Remarkably, an approximately 8.9-fold improvement in H_2 production was achieved with this approach compared to pristine g-C_3N_4. The enhanced performance is attributed to changes in the electronic structure and charge carrier behavior of g-C_3N_4 facilitated by the in situ growth of a NiS-WO_3 heterojunction system. The NiS-assisted WO_3/g-C_3N_4 heterojunction introduces additional active sites that promote efficient charge separation and transfer processes. When NiS is employed as a co-catalyst in the system, the H_2 evolution reaction rate significantly increases, reaching 2929.1 μmol g^{-1} h^{-1} under visible light irradiation.

Xu et al. (2019) [57] enhanced H_2 production by water splitting using NiCoP as a co-catalyst to decorate g-C_3N_4, which was also hybridized with montmorillonite (MMT). The resulting MMT/g-C_3N_4/NiCoP composites achieved a significantly higher H_2 evolution rate of 12.50 mmol h^{-1} g^{-1} at pH 11 with 1.0 mmol L^{-1} eosin Y (EY) sensitization, outperforming MMT/g-C_3N_4 and g-C_3N_4/NiCoP composites. The photocatalytic performance of g-C_3N_4 was improved through hybridization with MMT and NiCoP as the co-catalyst. The highest H_2 evolution rate observed was 12.50 mmol h^{-1} g^{-1} for MMT/g-C_3N_4/15%NiCoP under visible light, which was 26 times higher than MMT/g-C_3N_4 (0.48 mmol h^{-1} g^{-1}) and 1.6 times higher than g-C_3N_4/15%NiCoP (7.69 mmol h^{-1} g^{-1}). The AQY at 420 nm reached 40.3%. This significant improvement was attributed to the enhanced dispersion of g-C_3N_4 layers, the staggered conduction band potentials between g-C_3N_4 and NiCoP, and the electrostatic repulsion from negatively charged MMT. This study demonstrates that MMT is an excellent support for catalytically active components in photocatalytic H_2 production. Dye sensitization enhances a photocatalyst's absorption in the visible-light region. However, for effective H_2 generation, the dye must remain stable, and efficient co-catalysts are needed to facilitate electron transfer from excited dye molecules to active sites. One way to stabilize the dye is by immobilizing it on a porous support. Noble metals like platinum (Pt) are common co-catalysts that improve electron transfer, while transition metal phosphides are also promising due to their abundance and ability to capture photoinduced charges in non-dye-sensitized photocatalysts.

Gao et al. (2019) [39] synthetized g-C_3N_4@TiATA composites of Ti-MOFs (TiATA) and metal-free graphitic carbon nitride (g-C_3N_4), forming a heterostructure between g-C_3N_4 and TiATA. The development of heterostructured photocatalysts is an effective approach to improve H_2 production from water splitting due to enhanced charge transport efficiency. This heterojunction not only extends the light absorption range of g-C_3N_4@TiATA to 490 nm, compared to 456 nm for pure g-C_3N_4, but also significantly accelerates charge migration. Photocatalytic experiments reveal that the heterostructure effectively steers charge flow from g-C_3N_4 to TiATA, and subsequently to Pt nanoparticle co-catalysts, achieving a remarkable photocatalytic H_2 production rate of 265.8 μmol h^{-1} under a 300 W Xenon lamp, which is about 3.4 times higher than that of g-C_3N_4/Pt.

Huang et al. (2019) [58] synthesized a 3D hollow-sphere structure of graphitic carbon nitride (g-C_3N_4) with a large specific surface area and high porosity. This hollow-sphere

structure serves as an effective substrate for the uniform dispersion of Pd nanoparticles, improving visible light absorption and exposing more active sites. Pd nanoparticles, acting as electron acceptors, are incorporated into g-C_3N_4, which increases the material's ability to trap transition electrons, thereby boosting the number of photogenerated charge carriers involved in surface reactions. The Pd/SCN composite showed outstanding photocatalytic H_2 evolution performance under visible light irradiation, with the H_2 production rate of Pd/SCN (10 h) reaching 267.9 μmol/h—nearly 10 times higher than that of Pd/2D g-C_3N_4. The photocatalytic H_2 evolution reaction was carried out in a 250 mL quartz reactor using a 300 W Xe lamp with a 400 nm UV cut-off filter to simulate natural sunlight. For each reaction, 50 mg of catalyst was dispersed in 100 mL of a 9:1 water/triethanolamine (TEOA) mixture. The reactor was evacuated for 30 min to remove air before starting the reaction.

Yi et al. (2024) [41] successfully covalently bonded three COFs (BDA-HTA-COF, BDA-DHTA-COF, and BDA-THTA-COF) with In_2O_3 for the first time to create a heterojunction. The resulting BDA-THTA-30 exhibits the greatest photocatalytic H_2 production activity of 9691.84 μmol g^{-1} h^{-1}, significantly surpassing BDA-THTA-COF and In_2O_3 by 10.1 and 128.3 times, respectively. Additional research indicates that covalent bonding between In_2O_3 and the elements of BDA-THTA-COF can greatly enhance the separation and transfer rate of light-induced charges in the composites, resulting in improved H_2 evolution activity.

Huang et al. (2024) [59] presented a novel synthesis method for the innovative atomic-level composite semiconductor photocatalyst CdNCN under mild conditions, while also clarifying its formation mechanism. By efficiently utilizing the $[NCN]^{2-}$ group in the thiourea method, they successfully performed the one-pot synthesis of CdNCN-CdS heterostructure photocatalysts. Significantly, the best-performing CdNCN-CdS sample shows an H_2 evolution rate of 14.7 mmol g^{-1} h^{-1} when exposed to visible light, making it the most effective catalyst compared to all other reported CdS-based composites lacking any co-catalysts. The remarkable H_2 evolution performance of CdNCN-CdS mainly stems from two crucial factors: (i) the formation of an atomic-scale N-Cd-S heterostructure at the junction of CdNCN and CdS, which enhances efficient electron transfer; (ii) the guided movement of electrons to the (110) crystal plane of CdNCN, which promotes optimal H_2 adsorption and effective involvement in the H_2 evolution reaction.

Yang et al. (2023) [60] successfully fabricated neodymium iron composites made up of NdOCl/Fe_2O_3/$NdFeO_3$, which have a platelet-like nanostructure. They investigated the effects of changes in phase composition due to varying annealing temperatures (750 to 900 °C). The sample obtained at an annealing temperature of 800 °C showed the greatest photocatalytic H_2 evolution rate of 12.79 μmol g^{-1} h^{-1} with methanol as the sacrificial agent and 18.99 μmol g^{-1} h^{-1} with triethanolamine (TEOA), respectively. They also proposed a potential mechanism involving the separation of photogenerated charge carriers due to different interfacial heterojunctions resulting from the different phase compositions of each sample.

Major Achievements in the Development of the Z-Type Heterojunction Photocatalytic Composites for Photocatalytic H_2 Production

The synthesis of photocatalytic materials for hydrogen production has seen significant advances in recent years, as researchers seek to improve efficiency by addressing common issues such as electron–hole recombination, photocorrosion, and limited light absorption. Xie et al. (2025) [48] pioneered a novel Z-type heterojunction, Pt/$Zn_{0.2}Cd_{0.8}S$/$Cs_3PW_{12}O_{40}$, which effectively reduces photocorrosion and enhances charge carrier separation, demonstrating a promising photocatalytic H_2 production rate of 10.4 mmolg^{-1} h^{-1}. However, creating stable, atomic-scale semiconductor heterojunctions remains a significant challenge. In a different approach, Li et al. (2021) [49] created CdS/$ZnIn_2S_4$ heterojunctions with epitaxial growth, pushing the limits of photocatalyst design at the atomic level. This approach

illustrates the ongoing difficulty of synthesizing highly efficient and stable heterojunctions that can effectively manage electron migration.

Meanwhile, $MnPS_3$, known for its strong visible light absorption, suffers from high electron–hole recombination and insufficient oxidation capacity, though recent developments like the $MnPS_3$-$Cs_4W_{11}O_{35}$ composite have significantly enhanced its H_2 production rate by nearly three times [50]. This illustrates the importance of overcoming inherent material limitations, such as recombination rates and oxidation capabilities, which hinder the performance of promising photocatalysts like $MnPS_3$. The incorporation of nonmetallic elements, such as boron in $CoMoO_4$, is another example of progress, with Li et al. (2025) [51] demonstrating that B/$CoMoO_4$ outperforms its non-doped counterpart, achieving a remarkable H_2 production rate of 7460 μmol g^{-1} h^{-1}. This highlights how modifying the electronic properties of catalysts can lead to substantial improvements in photocatalytic efficiency.

The development of p–n heterojunctions, as seen in the CuS/$NaNbO_3$ system (Chang et al., 2023) [52], provides an effective strategy to enhance photocatalytic performance by preventing charge carrier recombination. Similarly, Fang et al. (2023) [53] hybridized TiO_2 with $Co_{1.29}Ni_{1.71}O_4$, achieving a 26.7-fold enhancement in H_2 production. These materials benefit from enhanced charge separation and light absorption, showcasing the critical role of heterojunction design in boosting photocatalytic efficiency. Wu et al. (2021) [55] achieved a similar outcome with a Co_3O_4/CdS/g-C_3N_4 ternary composite, which showed a dramatic increase in H_2 production, further confirming the power of synergistic material combinations for improving photocatalytic performance.

However, these advances are not without their drawbacks. For example, while the NiS/WO_3/g-C_3N_4 composite [56] achieved significant improvement in H_2 production, the dye sensitization process requires stable dyes and efficient electron transfer to the active sites for optimum performance, presenting a challenge for long-term stability. Additionally, Gao et al. (2019) [39] developed a TiATA@g-C_3N_4 heterostructure to enhance H_2 production, but the increase in light absorption and charge migration efficiency is still limited by material stability and the scalability of the synthetic process.

Despite these challenges, the continued development of novel heterostructures, the use of co-catalysts, and atomic-level design of composites show promise in overcoming existing limitations, offering a pathway for more efficient and stable photocatalytic systems. The key to future success lies in addressing stability issues, reducing recombination rates, and improving material scalability to enable real-world applications of photocatalytic hydrogen production.

3.5.3. MXene as a New Class of Two-Dimensional (2D) Metal Carbides, Nitrides, or Carbonitrides

A critical step in photocatalytic H_2 evolution is the effective separation of the photogenerated charge carriers. Noble metals, particularly platinum (Pt), are commonly employed to enhance charge carrier separation efficiency, thereby boosting photocatalytic H_2 production. However, due to concerns over the high cost and limited availability of Pt, MoS_2 has emerged as a competitive alternative. Semiconductor–MoS_2 hybrids offer remarkable advantages for photocatalytic H_2 evolution in certain applications, providing potential benefits over semiconductor–Pt hybrids. Furthermore, MXene, a new class of two-dimensional (2D) metal carbides, nitrides, or carbonitrides, has attracted considerable attention in various fields such as batteries, supercapacitors, and sensors. Its unique properties, including excellent metallic conductivity, chemical versatility, and structural stability, make it a highly competitive material for use as a catalyst support in photocatalysis.

The recently developed MXene photocatalytic composites for photocatalytic H_2 production are listed in Table 3. Zheng et al. (2021) [61] developed $CdxZn_{1-x}S/Ti_3C_2$ ultrathin

MXene composites using a simple electrostatic assembly method. The unique 0D/2D structure of these composites exhibited significantly improved photocatalytic H_2 production performance compared to bare $CdxZn_{1-x}S$. Spectroscopic analyses confirmed that the electronic interactions and the Schottky barrier formed at the interface between $CdxZn_{1-x}S$ and Ti_3C_2 MXene play a crucial role in promoting the efficient separation of photoinduced electron–hole pairs. The successful implementation of electrostatic self-assembly to integrate $CdxZn_{1-x}S$ with ultrathin MXene paves the way for utilizing electrical differences and band theory to design rational semiconductor/MXene Schottky structures for various photocatalytic applications.

Table 3. Recently developed MXene photocatalytic composites for photocatalytic H_2 production.

MXene Photocatalytic Composites	Advantage	H_2 Production	Ref.
0D/2D structure of $CdxZn_{1-x}S/Ti_3C_2$ ultrathin MXene composites Ti_3C_2 MXene, CZS, and CZS/Ti_3C_2 MXene composites	λ > 420 nm, 300 W Xe lamp, 70 mL deionized water and 30 mL of a sacrificial agent mixture (Na_2S and Na_2SO_3) in a 1:1 volume ratio, Na_2S/Na_2SO_3 as sacrificial agents	bare CZS–5.56635 mmol g^{-1} h^{-1} CZS/Ti_3C_2 MXene composites (Ti_3C_2 content 1 wt%)–15.03581 mmol g^{-1} h^{-1}	[61]
Binary heterojunction photocatalyst, consisting of $Cd_{0.5}Zn_{0.5}S$ nanorods on 0.5 wt% Ti_3C_2 MXene nanosheet	λ = 350 nm	15.56 mmol g^{-1} h^{-1}	[62]
Ti_3C_2 MXene@$TiO_2/ZnIn_2S_4$ (MXene@TiO_2/ZIS)	300 W Xeon lamp Na_2S/Na_2SO_3 as sacrificial agents	1.1858 mmol g^{-1} h^{-1}	[63]
Ti_3C_2Tx MXene-based composites Ti_3C_2 MXene 6.7 wt% dispersion modified with tetraethyl hydroxyl ammonium (TEHA) alongside rhombic-shaped TiO_2 nanoparticles		0.39092 mmol h^{-1}	[64]
g-C_3N_4 nanotube@polydopamine(pDA)/NiCo-LDH (LPC) composite	λ > 420 nm, Triethanolamine (TEOA) as the hole-capturing reagent	1.5551 mmol h^{-1} g^{-1}	[65]
CdS–BiOCl/PAN composites	lactic acid as a sacrificial agent, 300 W Xenon lamp	CdS powder–0.38948 mmol g^{-1} h^{-1} 0.09753 mmol g^{-1} h^{-1} during the second cycle CdS–BiOCl/PAN composites-C–B–P(3) > C–B–P(2) > C–B–P(1) > C–B–P(4) > C–B–P(5): 0.28865, 0.24371, 0.21504, 0.20763, and 0.15618 mmol g^{-1} h^{-1} BiOCl/PAN–0.03601 mmol g^{-1} h^{-1}	[66]

Photocatalytic H_2 production was evaluated using an online photocatalytic evaluation system under visible light irradiation from a 300 W Xe lamp equipped with a 420 nm cut-off filter. Typically, 10 mg of each prepared sample was dispersed in 100 mL of solution consisting of 70 mL of deionized water and 30 mL of a sacrificial agent mixture (Na_2S and Na_2SO_3) in a 1:1 volume ratio. Cooling water was circulated through the reactor to

maintain the temperature at 5 °C. The amount of H_2 produced was analyzed using gas chromatography with a thermal conductivity detector (TCD).

The photocatalytic H_2 evolution properties of Ti_3C_2 MXene, CZS, and CZS/Ti_3C_2 MXene composites were investigated under visible light irradiation using 0.35 M Na_2S and 0.25 M Na_2SO_3 as sacrificial agents. Ti_3C_2 MXene exhibited metallic properties and supported its role as a co-catalyst rather than a photocatalyst. The H_2 evolution rate of bare CZS was found to be 5566.35 μmol g^{-1} h^{-1}. In contrast, the H_2 production activity of CZS/Ti_3C_2 MXene composites improved significantly upon the coupling of Ti_3C_2 MXene, showing an initial increase followed by a decrease in activity. When the Ti_3C_2 content reached 1 wt%, the composite achieved the highest H_2 production rate of 15,035.81 μmol g^{-1} h^{-1}, which is 2.7 times greater than that of bare CZS. However, as the Ti_3C_2 MXene content increased further, the photocatalytic activity gradually declined. This reduction in activity is attributed to several factors, including the coverage of active sites by excess Ti_3C_2 MXene and the formation of recombination centers for photogenerated charge carriers due to the high loading of Ti_3C_2 MXene.

Li et al. (2024) [62] prepared a binary heterojunction photocatalyst, consisting of $Cd_{0.5}Zn_{0.5}S$ nanorods on a Ti_3C_2 Mxene nanosheet. In the composite material, the $Cd_{0.5}Zn_{0.5}S$ nanorods are evenly coated across the surface of the single-layer Ti_3C_2 nanosheets, creating a Schottky heterojunction at the interface of the materials. This arrangement improves the efficiency of separating photogenerated electrons and holes, thus boosting light utilization. By incorporating 0.5 wt% (mass fraction) of Ti_3C_2 MXene, they noted a maximum photocatalytic H_2 generation rate of 15.56 mmol g^{-1} h^{-1}, which surpassed the baseline $Cd_{0.5}Zn_{0.5}S$ by 2.56 times. Significantly, photocatalytic efficiency stayed mostly the same following five cycles. This composite reached the highest apparent quantum efficiency of 18.4% under 350 nm UV light exposure. This study illustrates the efficacy of the innovative carbon-based material MXene as a co-catalyst to enhance the functionality of photocatalysts and presents a practical method for developing photocatalytic H_2 evolution catalysts containing MXene. The fabrication of Ti_3C_2Tx Mxene-based composites, with precise control over size, shape, and surface properties for high-efficiency photocatalytic applications, is promising and challenging. Two-dimensional MXene materials are promising candidates for co-catalysts due to their hydrophilicity, photostability, extensive specific surface area, and excellent conductivity. Ti_3C_2 MXene is a promising option for a co-catalyst, that could replace noble metals in photocatalytic H_2 generation. Ti_3C_2 acts as a co-catalyst that effectively reduces the recombination of photogenerated electrons and holes, enhancing catalytic efficiency. Thanks to its low cost, non-toxic nature, and plentiful availability of TiO_2 and Ti_3C_2, this stable composite is anticipated to function as a photocatalyst for extensive applications.

Huang et al. (2020) [63] developed a novel hierarchical Ti_3C_2 MXene@TiO_2/$ZnIn_2S_4$ (MXene@TiO_2/ZIS) photocatalyst with rapid charge transfer channels using a two-step hydrothermal method for efficient H_2 production. The approach involved hydrothermal oxidation for in situ synthesis of Ti_3C_2 MXene embedded with TiO_2 nanosheets (M@TiO_2), which were subsequently used as a support for $ZnIn_2S_4$ (ZIS). The optimized hybrid photocatalyst exhibited an H_2 production rate of 1185.8 μmol g^{-1} h^{-1}, which was 9.1 times higher than that of M@TiO_2 and 4.6 times higher than that of pure ZIS. The improved photocatalytic performance was attributed to the enhanced light absorption capabilities of ZIS and Ti_3C_2, the abundant active sites of Ti_3C_2, the strong interfacial interactions, and the efficient separation and transport of photogenerated charge carriers enabled by the heterojunction. Key charge transfer pathways included the type II heterojunction formed between ZIS and TiO_2 nanosheets, the Schottky junction between Ti_3C_2 and the semiconductor, and the excellent conductivity of metallic Ti_3C_2. This study confirmed

the formation of Schottky junctions between ZIS and Ti_3C_2 and emphasized that the hierarchical M@TiO_2 structure acts as both a beneficial platform and an effective co-catalyst, facilitating the further development of MXene-based photocatalysts.

Zong et al. (2022) [64] fabricated Ti3C2–TiO2 composites by a two-phase assembly technique using Ti_3C_2 Mxene dispersion modified with tetraethyl hydroxyl ammonium (TEHA) alongside rhombic-shaped TiO_2 nanoparticles that feature exposed {101} facets. The Ti_3C_2 Mxene serves as an effective support for anchoring TiO_2 nanoparticles with a size of 15 nm and excellent facet regulation. The Ti3C2–TiO2 composites achieve significantly improved photocatalytic H_2 evolution activity. The maximum H_2 production rate of 390.92 μmol h^{-1} is achieved with the Ti3C2–TiO2 composites at a Ti_3C_2 of 6.7 wt%, which is 2.1 times higher than that of pure TiO_2. This remarkable photocatalytic performance can be attributed to the increased light absorption, enhanced charge separation efficiency, and available {101} facets in the TiO_2 nanoparticles. This study presents a novel approach to prepare high-quality MXene Ti3C2–TiO2 hybrids with strong photocatalytic properties, which could be widely utilized to prepare other MXene-derived composites with outstanding properties.

Meng et al. (2021) [65] develop a novel g-C_3N_4 nanotube@polydopamine(pDA)/NiCo-LDH (LPC) composite photocatalyst by integrating hydrothermal and calcination techniques. In the LPC composite system, the one-dimensional (1D) g-C_3N_4 nanotubes, with their larger specific surface area, provide more active sites and help to reduce the charge migration distance, while the rapid mass transfer in the nanotubes can speed up the reaction process. The g-C_3N_4/NiCo-LDH type II heterojunction can effectively promote the spatial separation of charge generated by light. Furthermore, pDA acts as a metal-free heterojunction interface medium that offers various actions (π-π* electron delocalization effect, adhesive properties, and photosensitization). The optimized LPC nanocomposite shows approximately 3.3 times greater photoactivity for H_2 production compared to the g-C_3N_4 nanotube when exposed to solar light. Moreover, the results from the cyclic experiments indicate that the LPC composite photocatalyst demonstrates excellent stability and recyclability. The resulting g-C_3N_4@pDA/NiCo-LDH composite photocatalyst exhibits potential real-world applications in energy conversion.

Zhang et al. (2019) [66] developed CdS–BiOCl/PAN composites for H_2 production under UV–vis light, benefiting from the synergy between CdS, BiOCl, and PAN. The CdS content in the composites was the key to their photocatalytic performance. Bismuth oxyhalides (BiOX, X = Cl, Br, I) have gained attention as photocatalysts due to their unique layered structure, which reduces electron–hole recombination and boosts efficiency. Pure BiOCl/PAN absorbed only UV light, with an absorption edge at 370 nm, while CdS absorbed visible light with an edge near 614 nm. The CdS–BiOCl/PAN composites showed a shift in absorption to longer wavelengths, with stronger absorption in the 300–600 nm range, indicating that CdS incorporation improved the photocatalytic performance of BiOCl/PAN. Photocatalytic H_2 production was carried out using a 5 mg sample dispersed in 50 mL of solution containing 5 mL of lactic acid as a sacrificial agent and irradiated by a 300 W Xenon lamp. The system was evacuated for 60 min before the reaction to ensure vacuum conditions. The CdS powder had the highest H_2 evolution rate (389.48 μmol g^{-1} h^{-1}), but its activity quickly declined in subsequent cycles, dropping to 97.53 μmol g^{-1} h^{-1} due to poor recyclability. In contrast, the CdS–BiOCl/PAN composites showed higher H_2 production rates than pure BiOCl/PAN (36.01 μmol g^{-1} h^{-1}), which can be attributed to CdS incorporation and the formation of a heterojunction structure. As the CdS content increased, the photocatalytic performance of the CdS–BiOCl/PAN composites improved, peaking at C–B–P(3). This indicates that the CdS–BiOCl heterojunction was most effective at this composition. However, beyond a certain CdS threshold, excess CdS

nanoparticles agglomerated into larger particles, which acted as recombination centers for photogenerated electron–hole pairs, reducing photocatalytic efficiency. The photocatalytic activity of C–B–P(3) remained stable after six cycles, showcasing its excellent chemical stability. This stability can be attributed to the synergistic effects of CdS, BiOCl, and PAN in the C–B–P(3) composite.

Wang et al. [8] synthesized nitrogen-doped carbon CdS@NC composites through the carbonization of a crystalline complex consisting of cadmium cations and methyl orange anions, $[Cd(H_2O)_6(C_{14}H_{14}N_3SO_3)_2]1$. These composites were explored as efficient photocatalysts for enhanced H_2 production under visible light irradiation ($\lambda \geq 420$ nm), achieving a remarkable H_2 evolution rate of approximately 7428.0 μmol h^{-1} g^{-1}. This rate is relatively high compared to previously reported CdS-based nanomaterials. In this study, ref. [8], CdS@NC composites were synthesized using a one-step in situ carbonization strategy involving a pre-assembled crystalline cadmium complex, $[Cd(H_2O)_6(C_{14}H_{14}N_3SO_3)_2]$ (methyl orange = $C_{14}H_{14}N_3SO_3Na$). This complex consists of cadmium cations and methyl orange (MO) anions arranged into supramolecular scaffolds. It was found that cadmium and sulfur species in the precursors formed CdS nanoparticles (NPs), which were simultaneously deposited on nitrogen-doped carbon (NC) scaffolds during the high-temperature carbonization process and the formation of CdS@NC composites. Among these, the optimal CdS@NC–500–4 composite showed outstanding photocatalytic H_2 evolution, achieving a rate of 7428.0 μmol h^{-1} g^{-1} in an aqueous Na_2S/Na_2SO_3 system (as sacrificial reagents). In comparison, the reference material *CdS@NC–500–4, obtained by physically mixing $Cd(NO_3)_2{\cdot}4H_2O$ and MO and then carbonizing, exhibited a significantly lower H_2 evolution rate of 1300.9 μmol h^{-1} g^{-1}. These results indicate that combining Cd^{2+} and MO anions into a crystalline phase is essential for optimizing the photocatalytic performance of the resulting composites. Under the given conditions, the pristine crystalline complex 1 produced a negligible H_2 rate of 19.2 μmol h^{-1} g^{-1}. After carbonization, CdS@NC photocatalysts showed significant improvements, with H_2 production rates ranging from 357.7 μmol h^{-1} g^{-1} for CdS@NC–500–1 to 7428.0 μmol h^{-1} g^{-1} for CdS@NC–500–4. In contrast, the reference material *CdS@NC–500–4, made by carbonizing a mixture of $Cd(NO_3)_2{\cdot}4H_2O$ and MO, had a lower rate of 1300.9 μmol h^{-1} g^{-1}. The enhanced photocatalytic activity was mainly due to the carbonization temperature, which narrowed the bandgap, improved light absorption, and facilitated charge separation. CdS@NC–500–4 showed the best performance, attributed to the effective interfacial contacts between CdS nanoparticles and nitrogen-doped carbon supports. All CdS@NC materials outperformed pure CdS in H_2 production. Stability studies of CdS@NC–500–4 revealed that the photocatalyst maintained its efficiency over a 25-h period (monitored at 5-h intervals) without significant decreases in activity. PXRD analysis confirmed that the phase purity and crystallinity of CdS@NC–500–4 remained stable even after prolonged photocatalytic use.

Major Achievements in the Development of MXene-Based Composites for Photocatalytic H_2 Production

Recent studies have focused on materials like MoS_2, MXenes, and other semiconductor hybrids, which show promising results in improving photocatalytic H_2 production while addressing the cost and sustainability concerns associated with platinum-based systems.

The incorporation of MoS_2 into semiconductor composites has demonstrated notable advantages. MoS_2, with its layered structure, offers excellent charge transfer properties and can effectively enhance the photocatalytic performance of semiconductors like $CdxZn_{1-x}S$. The research by Zheng et al. (2021) [61] showed that the integration of $CdxZn_{1-x}S$ with Ti_3C_2 MXene, a 2D material, resulted in significant improvements in photocatalytic H_2 production, with the Ti_3C_2 hybrid exhibiting 2.7 times greater efficiency than pure $CdxZn_{1-x}S$.

This is attributed to the Schottky junction formed at the interface, which plays a crucial role in facilitating efficient charge separation. Moreover, the use of MoS_2-based composites, as observed in the study, presents a sustainable alternative to Pt while maintaining high performance.

MXenes, especially Ti_3C_2, have also attracted significant attention as catalyst supports. Ti_3C_2 MXene has excellent metallic conductivity, hydrophilicity, and structural stability, making it a strong candidate for enhancing photocatalytic reactions. In the work of Li et al. (2024) [62], the $Cd0.5Zn_{0.5}S/Ti_3C_2$ composite exhibited a remarkable 2.56-fold enhancement in photocatalytic H_2 production compared to bare $Cd0.5Zn_{0.5}S$. This was attributed to the efficient separation of charge carriers enabled by the Schottky heterojunction between $Cd0.5Zn_{0.5}S$ and Ti_3C_2. The stability and recyclability of Ti_3C_2-based composites were further demonstrated by the fact that the composite maintained its efficiency over multiple cycles, emphasizing the potential of MXenes in practical applications. Similarly, other Ti_3C_2-based composites, such as $Ti_3C_2@TiO_2/ZnIn_2S_4$ [63], also showed substantial improvements in photocatalytic H_2 production by facilitating charge transfer through various heterojunctions, including type II junctions between TiO_2 and $ZnIn_2S_4$ and Schottky junctions between Ti_3C_2 and the semiconductor.

Despite the impressive performance of Ti_3C_2-based composites, challenges still remain, particularly with the optimal loading of Ti_3C_2. Zheng et al. (2021) [61] found that while a 1 wt% loading of Ti_3C_2 in the composite resulted in the highest photocatalytic activity, further increases in Ti_3C_2 content led to a decline in performance. This reduction was attributed to the excessive coverage of active sites by Ti_3C_2 and the formation of recombination centers for photogenerated charge carriers, highlighting the importance of optimizing Ti_3C_2 loading to achieve the best photocatalytic performance. This is a common issue faced by many photocatalytic systems where excessive loading of the support material can hinder the active sites' exposure and charge transfer efficiency.

Another key factor in improving photocatalytic performance is the enhancement of light absorption. The study by Zong et al. (2022) [64] demonstrated that Ti3C2–TiO2 composites achieved a 2.1-fold increase in H_2 production due to the improved light absorption and charge separation facilitated by the unique exposed {101} facets of TiO_2 nanoparticles. This facet-specific design improved the photocatalytic efficiency of the composite, showing that the structural modification of semiconductor materials plays an essential role in optimizing photocatalysis.

In addition to the structural and material improvements, the stability of the photocatalysts is a crucial aspect for large-scale applications. The work by Meng et al. (2021) [65] on $g\text{-}C_3N_4$/NiCo-LDH composites showed that the integration of polydopamine (pDA) as a metal-free heterojunction interface material effectively enhanced charge migration and resulted in a photocatalyst with excellent stability and recyclability. The $g\text{-}C_3N_4$@pDA/NiCo-LDH composite demonstrated a 3.3 times greater H_2 production rate than pure $g\text{-}C_3N_4$, while maintaining its activity over multiple cycles. This stability, along with the enhancement in photocatalytic activity, highlights the potential for composites to operate over extended periods without significant degradation.

While the results are promising, there are several challenges that need to be addressed to move these materials from laboratory-scale systems to industrial applications. The stability of Ti_3C_2-based composites in aqueous environments remains a concern, as the high reactivity of Ti_3C_2 in water may lead to material degradation over time. Similarly, the scalability of synthesis methods for MXenes, MoS_2, and other composites is an important consideration. While techniques like electrostatic assembly and hydrothermal processes offer good control over material composition, they may not be easily scalable for large-scale production. The cost of these materials, though lower than platinum, can still be a limiting

factor, especially when considering the need for high-quality materials and precise control over their synthesis.

Additionally, while composites like CdS@NC, as reported by Wang et al. (2021) [8], have shown excellent photocatalytic performance, there is still a need for optimization in terms of material design. The carbon-based support material in these composites significantly improved photocatalytic activity, but the challenge lies in ensuring that the carbon content does not adversely affect the material's performance in the long term. Furthermore, the ability to tailor the surface properties and interfaces of these composites for maximum charge separation efficiency remains a key area for future research.

In conclusion, the integration of MXenes, MoS_2, and other semiconductor materials represents a significant advancement in the development of photocatalysts for hydrogen production. The demonstrated improvements in charge separation, light absorption, and stability show that these materials are highly competitive alternatives to traditional platinum-based photocatalysts. However, challenges, such as optimizing material loading, improving long-term stability, and scaling up synthesis methods, must be addressed for these materials to be viable for industrial applications. Future research should focus on enhancing the scalability of synthesis processes, improving the stability of MXene-based and MoS_2-based composites, and refining the material design to maximize photocatalytic efficiency. With continued advancements, these materials hold the potential to play a critical role in the development of sustainable hydrogen production systems.

4. Interfacial Charge Separation and Transfer in Composite Photocatalysts

The interaction between components in composite photocatalysts plays a critical role in determining their efficiency by affecting the movement of photogenerated charge carriers. While much research has focused on incorporating upconversion materials to extend light absorption into the long-wavelength spectrum, the role of interfacial properties in optimizing performance remains underexplored. One challenge is facilitating efficient charge transfer between non-conductive upconversion materials and semiconductors [1].

The development of composite photocatalysts with suitable material combinations not only broadens the light absorption spectrum but also improves the separation of photogenerated charge carriers. Upconversion materials have the distinctive ability to convert long-wavelength near-infrared (NIR) light into shorter-wavelength visible light so that NIR can be used to activate composite photocatalysts containing these upconversion agents. Among the various upconversion materials, lanthanide-doped hexagonal NaYF4 stands out due to its exceptional stability and low photon energy requirement. When excited by NIR light at around 980 nm [67], it emits mainly in the 540–560 nm range, making it ideal for integration with photocatalysts that have compatible bandgaps and similar hexagonal crystal structures, such as ZnO and CdS [1].

Additionally, molybdenite has emerged as an efficient co-catalyst, replacing platinum to improve electron–hole separation and enhance light absorption, thereby boosting photocatalytic activity. In particular, the PCN/Mo-2 composite demonstrated superior photocatalytic performance due to its excellent light absorption and effective charge carrier transfer [2]. The interface between g-C_3N_4 and molybdenite, formed through ball milling, plays a key role in ensuring efficient electron transfer. This interaction was crucial for the Pt-free photocatalytic activity of PCN/Mo-x composites, highlighting the importance of well-designed interfaces for effective charge separation [3]. Furthermore, the 2.0PCN-P25 composite also demonstrated improved photocatalytic activity due to the reduction in charge carrier recombination, facilitated by the coupling of CN with P25 and phosphorus doping, which lowered the bandgap and enhanced visible light absorption.

The significantly increased photocatalytic activity for H_2 generation under visible light is primarily attributed to the ability of the g-C_3N_4 nanotubes to provide numerous reaction sites and facilitate a reduction in charge carrier transport distances. Additionally, the fast mass transport within the nanotube can accelerate the reaction process, while the g-C_3N_4/NiCo-LDH type II heterojunction improves the spatial separation of the photoinduced charges. Furthermore, pDA serves as a metal-free interface medium for heterojunctions and provides various functions such as electron delocalization effect, adhesive properties and photosensitization [65]. Transient photocurrent response measurements, experiments with reactive oxygen species ($\cdot O_2^-$ and $\cdot$OH) and photoluminescence (PL) analyses provided evidence of strong electronic interactions between the defective CdS and ZnIn2S4, indicating enhanced charge separation and transport at the interface [49]. These results were further supported by DFT calculations, which confirmed improved charge transfer and electronic coupling within the heterojunctions.

Li et al. [54] observed an improvement in photocatalytic performance, which was attributed to two key factors: (1) the presence of carbon particles that facilitated the storage and transfer of electrons, and (2) the formation of a p–n heterojunction between Co_3O_4 and $Zn_xCd_{1-x}S$, which effectively promoted the separation of photogenerated charge carriers. Li et al. [54] showed that the incorporation of amorphous carbon and Co_3O_4 significantly improved electron and hole transfer while suppressing carrier recombination, providing favorable conditions for the development of highly efficient and stable C@$Zn_xCd_{1-x}S/Co_3O_4$ photocatalysts.

Manzoor et al. (2020) [16] used ZnO nanocomposites doped with varying concentrations of copper Cu (0.0, 0.01, 0.03, and 0.05 mol%) for photocatalytic H_2 production in a liquid-phase photoreactor with water–methanol splitting. A total of 1 g of photocatalyst particles were introduced into a water–methanol mixture within a 2-L Pyrex reactor. The reaction was performed at a wavelength of 365 nm. Their research showed that the incorporation of Cu into ZnO significantly improved the H_2 production rate from 7.49 μmol g^{-1} to 41.55 μmol g^{-1}. This enhancement is attributed to the effective reduction of electron–hole recombination during the photocatalytic reaction. Moreover, it was observed that Cu doping reduced the bandgap from 3.19 eV to 3.00 eV. Photoluminescence spectroscopy (PL) analysis showed that the recombination rate of photogenerated electrons and holes decreased with increasing Cu doping levels.

Enhancement in photocatalytic performance arises from two main factors. Firstly, the WO_3/g-C_3N_4 heterojunction effectively suppresses the recombination of photogenerated electron–hole pairs. Secondly, the incorporation of NiS improves electron mobility and introduces additional active sites that facilitate H_2 evolution [56].

Chen et al. (2019) reveal that increasing biochar content in biochar/$ZnFe_2O_4$ (BZF) composites improves H_2 evolution due to better electron transfer, but excessive biochar reduced the rate by blocking visible light absorption, lowering electron generation [47].

A short summary of experimental (e.g., XPS, PL, TRPL and ESR) evidence typically used to confirm the charge transfer mechanism, particularly for the very promising Z-scheme and S-scheme heterojunctions, is given in Table 4.

Table 4. A summary of the experimental techniques commonly used to confirm charge transfer mechanisms in Z-scheme and S-scheme heterojunctions in photocatalytic systems.

Experimental Technique	Purpose	Evidence
X-ray Photoelectron Spectroscopy (XPS)	Probes of the electronic structure and chemical states	• A directional shift in binding energies can indicate internal electric field formation and interfacial charge migration. • Work function measurements via XPS valence band analysis can support band alignment consistent with Z-scheme or S-scheme mechanisms.
Photoluminescence (PL) Spectroscopy	Measurement of the recombination of photogenerated charge carriers	• Lower PL recombination in heterojunction compared to single components indicates reduced recombination and supports effective charge separation.
Time-resolved Photoluminescence (TRPL)	Measurement of the carrier lifetime	• Longer carrier lifetimes in heterojunctions indicate efficient charge separation and transfer. • A complementary technique to the steady-state PL, which enables a temporal resolution of the charge dynamics.
Electron Spin Resonance (ESR)	Detection of the unpaired electrons, radicals, and trapped charge carriers	• Information on active electrons/holes, and indication which component is oxidized/reduced (e.g., in an S-scheme confirmation that electrons in the CB of the reductive semiconductor and holes in the VB of the oxidative semiconductor are retained).

5. Photocatalytic H_2 Production with Composite Photocatalysts

Zhu et al. (2022) [1] synthesized $NaYF_4$:Yb,Er/CdS composites using $NaYF_4$:Yb,Er nanorods and CdS nanoparticles through an ion adsorption/precipitation method and subsequent annealing under an argon atmosphere at varying temperatures to tune their microstructures. The annealing process facilitated the structural transformation from low-crystallinity cubic CdS to high-crystallinity hexagonal CdS, while also promoting improved interface contact between $NaYF_4$:Yb,Er and CdS. The study [1] showed that a robust interface between $NaYF_4$:Yb,Er and CdS greatly enhanced photocatalytic H_2 production. This improvement is likely attributed to the efficient charge transfer enabled by the optimized interface. Specifically, under light irradiation of $\lambda > 400$ nm the H_2 evolution activity increased from 171 to 2539 μmol h^{-1} g^{-1}, while under light irradiation of $\lambda > 600$ nm it improved from 0 to 19 μmol h^{-1} g^{-1}.

The PCN/molybdenite nanocomposites (PCN/Mo-x) exhibited a remarkable noble-metal-free photocatalytic H_2 evolution reaction rate under visible light [2]. The photocatalytic H_2 evolution reaction was conducted on a quartz glass under simulated light irradiation in a nitrogen-sealed environment. Typically, 100 mg of the photocatalyst was dispersed in 100 mL of a 0.75 M triethanolamine (TEOA) aqueous solution, with TEOA acting as the sacrificial agent. For bulk-PCN and PCN, 1 mL of H_2PtCl_6 aqueous solution was added to achieve a mass ratio of 3 wt% of Pt co-catalyst to photocatalyst, while H_2PtCl_6 was not added to the PCN/Mo-x and PCN/Mo-2 mixtures [2]. The setup was then degassed with high-purity nitrogen for 15 min to remove air completely and sealed with a quartz cover. The reactor was vertically irradiated with a 300 W Xe lamp, fitted with a

cut-off filter (λ > 420 nm), to provide visible light and reduce H_2PtCl_6 into the Pt co-catalyst. After purging with high-purity nitrogen again, the sealed reactor was irradiated with the same Xe lamp. The reaction was maintained at a constant temperature with circulating condensed water and conducted under magnetic stirring. The resulting H_2 production was measured using gas chromatography equipped with a 5A-zeolite column and a thermal conductivity detector. The photocatalytic activities of the samples were evaluated based on H_2 production from water splitting under simulated visible light irradiation. Stable and linear H_2 evolution rates were observed within 4 h for bulk-PCN and PCN in the presence of Pt (bulk-PCN/Pt and PCN/Pt, respectively), as well as for PCN/Mo-x without Pt [2]. Both bulk-PCN and PCN generated H_2 only after the incorporation of Pt nanoparticles, exhibiting H_2 evolution rates of 67 and 80 μmol g^{-1} h^{-1}, respectively. The improved performance of PCN was attributed to its enhanced specific surface area resulting from ball milling. Notably, even without the Pt co-catalyst, the PCN/Mo composites (PCN/Mo-1, 2, and 3) showed favorable H_2 evolution rates of 16, 27, and 19 μmol g^{-1} h^{-1}, corresponding to 23.9%, 40.3%, and 28.4% of the H_2 production rate of bulk-PCN/Pt, respectively [2].

All photocatalytic H_2 evolution experiments with CN, PCN, PCN-P25 and other CN/PCN-based composites were conducted at room temperature under simulated solar light conditions (irradiation provided by a 1000 W xenon lamp) using a 200 mL Pyrex quartz reactor [3]. In each typical experiment, 40 mg of the catalyst and 100 mL of a 10% methanol solution (as a sacrificial agent) were used. Prior to the reaction, the quartz reactor containing the methanol solution and catalyst was sonicated for 10 min and sealed with a silicone rubber septum to ensure airtight conditions. The system was then purged with N_2 gas for 10 min to establish an inert atmosphere. Following this preparation, the quartz reactor was exposed to simulated solar light irradiation, and the amount of H_2 gas evolved was quantitatively monitored on an hourly basis using a gas chromatograph (GC) instrument [3].

The photocatalytic performances of P25, CN, and PCN were individually assessed for their ability to produce H_2. Additionally, various weight percentages of CN and PCN composites with P25 were tested. The trend observed in photocatalytic H_2 production was as follows: CN < PCN < P25 < CN-P25 < PCN-P25. Among the different CN-P25 weight ratios, the 3.0CN-P25 composite exhibited the highest performance, with an optimal balance between photocatalytic activity and structural properties. Notably, increasing the CN content beyond 3% reduced performance due to the light-shielding effect of CN over the P25 surface. The 2.0PCN-P25 composite was identified as the optimal composition. The 3.0CN-P25 composite showed a nearly 22-fold increase in H_2 production (920 μmol/g) compared to CN alone (41 μmol/g) and a 10-fold increase compared to P25 alone (99 μmol/g), highlighting the significant enhancement achieved by optimizing the composite composition [3]. The 2.0PCN-P25 composite exhibited a nearly 40-fold increase in H_2 production (2531 μmol/g) compared to PCN alone and a 25-fold increase compared to P25 (99 μmol/g). A comparative analysis of CN, PCN, CN-P25, and PCN-P25 revealed that the 2.0PCN-P25 composite not only demonstrated the highest performance among all tested photocatalysts but also showed nearly three times greater H_2 production than the 3.0CN-P25 composite. This highlights the pivotal role of phosphorus doping in improving the performance of the composite photocatalyst [3].

Photocatalytic H_2 evolution experiments revealed that the optimal sample, hollow-sphere g-C_3N_4 (SCNO) SCNO/CoO (0.2), exhibited an impressive catalytic activity of 11,495 μmol H_2 h^{-1} g^{-1}, which was approximately four times higher than that of SCNN and two times higher than SCNO, and is attributed to the significantly enhanced rate of charge carrier transfer [7]. However, a reduction in the H_2 production rate was observed for SCNO/CoO (0.3), probably due to the agglomeration of CoO QDs. The photocatalytic

H_2 evolution reaction was performed in a 250 mL quartz reactor. A 300 W xenon (Xe) lamp equipped with a 420 nm ultraviolet cut-off filter was used as the visible light excitation source to simulate natural sunlight. Triethanolamine (TEOA) was used as the sacrificial agent to consume the photogenerated holes in the valence band. For each reaction, 50 mg of the synthesized photocatalyst was dispersed in 100 mL of a solvent mixture composed of water and triethanolamine (TEOA) in a volume ratio of 9:1. Prior to initiating the reaction, the reactor was evacuated for 30 min to ensure the complete removal of air. Hydrogen gas generation was analyzed using a gas chromatograph with argon as the carrier gas. To determine the (AQY), the measurements were carried out with a 420 nm band-pass filter and an optical power meter (NP2000-2) positioned 10 cm from the light exit port.

The photocatalytic H_2 evolution rate of SCNO was significantly higher than that of SCNN. This indicates that the wider pore structure and larger specific surface area of SCNO enhance its catalytic performance. Furthermore, the SCNO/CoO composite exhibited superior photocatalytic H_2 activity, highlighting the effectiveness of the novel one-step synthesis method to achieve highly dispersed CoO quantum dots (QDs) within the carbon nitride matrix. The large specific surface area of SCNO provided optimal conditions for the uniform distribution of CoO QDs. The results also showed that SCNO/CoO (0.2) outperformed CoO/g-C_3N_4 composites synthesized through a step-by-step method. The average particle size of CoO QDs on g-C_3N_4 was 5 nm, which was much smaller than the 30–50 nm CoO nanoparticles deposited on g-C_3N_4 using the step-by-step method. These smaller particles were uniformly dispersed over the g-C_3N_4 matrix, resulting in a higher number of active sites per gram of catalyst. This suggests that the reaction rate is proportional to the number of CoO QDs present on the support. The (AQY) of SCNO/CoO (0.2) was measured at 5.63% under the same experimental conditions using a 420 nm band-pass filter. Additionally, the AQY measurements were extended to other band-pass filters to assess the photocatalytic performance of SCNO/CoO (0.2) across a range of wavelengths. The results demonstrate that the SCNO/CoO (0.2) sample exhibits exceptional photocatalytic activity, outperforming most reported g-C_3N_4-based catalysts.

The photocatalytic H_2 evolution experiments for all samples are performed under visible light excitation ($\lambda > 420$ nm), using triethanolamine (TEOA) as the hole-capturing reagent. The photocatalytic performance of pure g-C_3N_4 is also lacking, with H_2 production merely reaching 58.1 μmol over 5 h, primarily due to the inadequate visible light absorption ability of the single-component photocatalytic material, leading to a rapid recombination of the photogenerated charge carriers. To address the aforementioned drawbacks, pDA has been deposited onto the surface of g-C_3N_4 nanotubes, which significantly increased the H_2 evolution activity of g-C_3N_4, with an H_2 evolution quantity reaching 121.3 μmol [65]. The enhanced rate of H_2 production results from two primary factors: firstly, the delocalization effect between pDA and g-C_3N_4 provides a driving force for the separation and movement of charge carriers. Secondly, the pDA exhibits enhanced electron transport ability, as it is closely wrapped around the surface of the g-C_3N_4 nanotubes, creating a larger contact area between them. This configuration provides numerous pathways for charge carrier transfer and effectively manages charge carrier recombination [65]. The photocatalytic performance of LDH/CN (292.6 μmol) has been evaluated to confirm that NiCo-LDH is a widely recognized photocatalytic substance in the photocatalytic arena, with its energy band alignment being suitable for g-C_3N_4 to create a type II heterojunction, thereby enhancing charge carrier separation and significantly boosting photocatalytic H_2 evolution activity [65]. The resulting LPC sample shows the maximum H_2 evolution activity of 398.7 μmol, approximately 1.4 times greater than that of LDH/CN. The amount of H_2 evolution for g-C_3N_4, CN@pDA, LDH/CN, and LPC increases linearly with the duration of light exposure, confirming that H_2 generation can be sustained for 5 h [65].

The H_2 evolution reaction (HER) rate of pure NiCo-LDH is negligible under visible light exposure, whereas the rates for pure g-C_3N_4, CN@pDA, LDH/CN, and LPC are 232.5, 485.4, 1170.5, and 1555.1 μmol h^{-1} g^{-1}, respectively [65]. In comparison, it is evident that LPC exhibits the highest HER (1555.1 μmol h^{-1} g^{-1}). Consequently, LPC can enhance the effective use of solar energy and photocatalytic efficiency [65]. The optimized LPC composite has the greatest photocatalytic efficiency, with its H_2 evolution reaction (HER) of LPC (1555.1 μmol h^{-1} g^{-1}) being about 6.7 and 3.2 times greater than that of g-C_3N_4 (232.5 μmol h^{-1} g^{-1}) and CN@pDA (485.4 μmol h^{-1} g^{-1}), respectively [65].

The CdS/$ZnIn_2S_4$ hybrids show superior photocatalytic H_2 production activity compared to pristine CdS [49]. After 4.5 h of light irradiation, H_2 production was 1.28 mmol/g for the pure CdS sample, while the pristine ZIS sample achieved an H_2 yield of 5.14 mmol/g. Under identical photocatalytic conditions, all CdS/ZIS-X heterojunctions exhibited enhanced H_2 production following the incorporation of ZIS. Notably, when the ZIS loading amount was increased to 0.3, the ZIS/CdS-0.3 heterojunction achieved the highest activity, producing 5.80 mmol/g—surpassing both pure CdS (1.28 mmol/g) and the pristine ZIS sample (5.14 mmol/g). However, further increases in the ZIS loading amount resulted in reduced H_2 production. This decline is attributed to the excessive ZIS coverage blocking active sites on the CdS surface, thereby hindering redox reactions and lowering overall efficiency. Additionally, introducing excessive ZIS reduced the light absorption capacity of CdS, which negatively impacted photocatalytic performance [49].

The photocatalytic H_2 generation activities of the Ti_3C_2 MXene@TiO_2/$ZnIn_2S_4$ (MXene@TiO_2/ZIS) photocatalysts [63] were assessed through water splitting under simulated sunlight illumination (300 W Xeon lamp). A sample of 15 mg of the synthesized photocatalyst was suspended in 80 mL of an aqueous solution containing 0.35 M $Na_2S{\cdot}9H_2O$ and 0.25 M Na_2SO_3. Before starting light irradiation, the solution was degassed by vacuum treatment. The pristine ZIS and M@TiO_2 materials exhibited low H_2 evolution rates, primarily due to inefficient charge separation and limited light absorption. In contrast, when ZIS was combined with M@TiO_2, the resulting M@T/ZIS composites showed a marked improvement in photocatalytic H_2 production, suggesting a synergistic effect between the Ti_3C_2 metallic co-catalyst, TiO_2 nanosheets, and ZIS nanosheets. For the M@T/ZIS composites with varying ZIS content, H_2 production increased proportionally with longer light irradiation, indicating the stable catalytic activity of the photocatalysts. Among these, the M@T/ZIS-50 composite exhibited the highest H_2 production rate. However, a further increase in ZIS content led to a decrease in H_2 evolution efficiency, which was attributed to a "light-shielding effect".

Li et al. (2020) [54] dispersed 10 mg of the catalyst in a 10 vol% lactic acid aqueous solution within a 62 mL quartz glass bottle and deaerated with N_2 for 10 min. The quartz bottle was then placed into a multi-channel reaction system and exposed to a 5 W LED lamp for 5 h. The H_2 production of the C@ZCS composite catalyst increased with higher glucose content. At 30% glucose by mass, the H_2 yield was 583.34 μmol, 2.8 times higher than pure ZCS. The carbon particles acted as electron acceptors, boosting H_2 production. However, as the glucose content increased further, H_2 production declined due to excessive carbon particles blocking ZCS active sites. Additionally, H_2 production rose with increased Co_3O_4 content, reaching a maximum of 1405.1 μmol for C@ZCS/CO30. The p–n heterostructure between Co_3O_4 and ZCS improved carrier separation, while carbon particles facilitated electron transfer. However, excessive Co_3O_4 reduced H_2 production by blocking ZCS active sites, limiting contact with reagents and water molecules. Hydrogen production also decreased due to lactic acid consumption.

Chen et al. (2019) [47] have studied the photocatalytic H_2 evolution by the biochar/$ZnFe_2O_4$ (BZF) composite, which was tested using a 300 W xenon lamp with

a UV cut-off filter (λ > 420 nm). A mixture of 0.02 g photocatalyst, 0.02 g Eosin Y photosensitizer, and 1 mL of triethanolamine (TEOA) in 20 mL aqueous solution was sonicated for 5 min. The reactor was purged with N_2 gas and irradiated for 30 min. The photocatalytic H_2 evolution of BZF composites, pure $ZnFe_2O_4$, and biochar (BC) was investigated under visible light over 3 h. A control with biochar alone showed no H_2 production, confirming that biochar is non-photosensitive and cannot generate photogenerated electrons. In contrast, BZF composites outperformed pure $ZnFe_2O_4$, which had a low H_2 evolution rate of 173 μmol g^{-1} h^{-1} due to the rapid recombination of electron–hole pairs. The BZF-5 composite, with the highest biochar content, achieved a rate of 1219 μmol g^{-1} h^{-1}, about six times that of pure $ZnFe_2O_4$ [47].

5.1. Apparent Quantum Efficiency (AQE) for H_2 Evolution

Li et al. (2021) [49] and Huang et al. (2019) [58] have used the following equation to calculate AQY for H_2 evolution:

$$AQY = \frac{\text{The number of evolved hydrogen molecules} \times 2}{\text{The number of incident photons}} \times 100\%$$

Li et al. (2021) [49] determined AQE using monochromatic LED light sources at wavelengths of 395, 420, 500, and 590 nm. The CdS/ZIS-0.3 heterojunctions exhibited a strong wavelength dependence, indicating that the H_2 production arises from the reduction of H_2O, driven by photoexcited electrons under light irradiation.

Huang et al. (2019) [58] performed measurements with a 400 nm band-pass filter and an optical power meter to determine the (AQY). The light source was positioned 10 cm from the light exit port. The AQY of Pd/SCN (10 h) was 3.52%, attributed to Pd nanoparticles embedded in g-C_3N_4 which provide abundant active sites for the water reduction reaction and enhance the separation of photogenerated electrons [58]. As the oil bath time increased to 10 h, the H_2 evolution rate correlated positively with the duration. However, for Pd/SCN (12 h), the rate decreased, likely due to Pd nanoparticle agglomeration. In contrast, Pd/SCN (10 h) outperformed Pd/BCN in H_2 production, likely due to SCN's larger surface area and porous hollow structure. The hollow-sphere structure of g-C_3N_4 offers more active sites and improves visible light absorption, while reduced surface area can negatively impact photocatalytic performance, underscoring the importance of surface area in efficiency.

Transient absorption (TA) spectroscopy is a powerful and reliable method for analyzing real-time photogenerated charge carriers and interfacial charge transfer dynamics in nanosystems. Suitable pump pulses can induce electron transitions from the valence band to the conduction band, allowing for the investigation of charge migration pathways. A 365 nm central wavelength was selected for the pump pulses [7].

Ying et al. [7] proposed the mechanism of photocatalytic H_2 production on SCNO/CoO composites based on experimental data carried out by transient absorption (TA) spectroscopy. During photocatalysis, electrons in the valence band (VB) of SCNO and CoO QDs are excited and migrate to their respective conduction bands (CB). The resulting electron holes are effectively scavenged by triethanolamine (TEOA). Because the CB of CoO QDs lies at a lower energy level than that of SCNO, photogenerated electrons preferentially transfer from SCNO to the CB of CoO QDs. The large specific surface area of CoO QDs provides a significant number of active sites, which accelerates the reaction rate and suppresses the recombination of photogenerated electrons and holes. Additionally, the defect energy levels within the CoO QDs play a crucial role. Some photogenerated electrons are trapped in these defect states, creating additional space for further photogenerated electrons and indirectly enhancing the number of electrons available for the reaction. These mechanisms collectively

suggest that the high photogenerated electron–hole pair separation rate in SCNO/CoO composites is a key factor leading to their superior photocatalytic H_2 evolution activity.

Chen et al. (2019) [47] proposed the mechanism for photocatalytic H_2 production using biochar/$ZnFe_2O_4$ (BZF) composite. In the photocatalytic H_2 evolution system, Eosin Y (EY) serves as a photosensitizer, being excited under light to form the singlet excited state (EY^{1*}), which then undergoes intersystem crossing (ISC) to the triplet excited state (EY^{3*}), a strong oxidant. The triplet state (EY^{3*}) is quenched by triethanolamine (TEOA), forming EY^- anions. These photogenerated electrons from the conduction band (CB) of $ZnFe_2O_4$ reduce protons from water to produce H_2. EY^- anions donate electrons to the conduction band of $ZnFe_2O_4$, enhancing photocatalytic H_2 evolution. Additionally, the photogenerated holes (h^+) in the valence band (VB) of $ZnFe_2O_4$ react with TEOA, promoting efficient electron–hole pair separation, as confirmed by previous photoluminescence (PL) and electrochemical impedance spectroscopy (EIS) studies. The presence of biochar in the BZF composites further boosts photocatalytic performance by facilitating rapid electron transfer from $ZnFe_2O_4$ to biochar, which aids in electron–hole separation and accelerates H_2 production. Additionally, the photogenerated holes (h^+) in the valence band (VB) of $ZnFe_2O_4$ can react with TEOA, facilitating the efficient separation of photogenerated electron–hole pairs. The presence of biochar in the BZF composites further enhances photocatalytic activity by effectively promoting the rapid transfer of photogenerated electrons from $ZnFe_2O_4$ to biochar. The electrons on the biochar's surface also participate in water reduction. Together, EY as a photosensitizer, TEOA as a sacrificial agent, and biochar as an electron mediator synergistically enhance the photocatalytic H_2 evolution efficiency of the BZF composite system.

5.2. Role of Sacrificial Agent

Although some photocatalysts are capable of evolving H_2 or O_2 in the presence of electron donors or acceptors (sacrificial reagents), the number of visible-light-driven photocatalysts that can split water into H_2 and O_2 without sacrificial reagents is still limited. Different compounds have been investigated as potential sacrificial agents, including methanol, ethanol and bio-available compounds such as ethanol, glycerol and sugars originating from biological substrates or wastes. The optimization of methanol concentration was performed using the optimized 2.0PCN–P25 composite under consistent experimental conditions, including fixed catalyst concentration and total solution volume, under simulated solar light irradiation. The methanol concentration was varied from 0% to 20% (V/V) [3]. It was observed that in the absence of methanol (0% methanol solution, i.e., pure water), the amount of H_2 production was significantly lower compared to solutions containing methanol. A 10% methanol solution exhibited the highest H_2 evolution capacity, with a production of 2531 μmol/g, confirming methanol's critical role as a sacrificial agent. Methanol acts by trapping the photogenerated holes from the semiconductor's valence band, thereby reducing the recombination of photogenerated electron–hole pairs and enhancing the efficiency of H_2 evolution [3]. However, increasing the methanol concentration beyond 10% led to a slight decrease in H_2 evolution efficiency. This decline is likely due to the formation of intermediate byproducts, such as CO_2 and methane, which consume photogenerated electrons and protons (H^+), thereby reducing the overall rate of H_2 production [3].

6. Additional Challenges in the Development of Photocatalytic Nanostructures and Composite Materials for H_2 Production

6.1. Effect of Annealing Temperature on Crystallinity

Zhu et al. [1] discovered that dispersion of CdS nanoparticles on NaYF4:Yb,Er nanorods and the strong interfacial interactions between the nanoparticles and nanorods enhanced photoluminescence (PL) emission. Compared to the unmodified NaYF4:Yb,Er, the photoluminescence (PL) emission peak of NaYF4:Yb,Er-380 remains centered around 550 nm, but its intensity is notably reduced by 80%. This reduction is attributed to the enhanced crystallinity achieved through annealing, which helps minimize the quenching of photogenerated charge carriers. The CdS and CdS-380 samples exhibit weak emission spectra with peaks at 640 nm and 780 nm, respectively. The 640 nm emission in CdS is due to its intrinsic bandgap emission, while the 780 nm emission in CdS-380 is linked to defect-related emissions. In the composite systems, NaYF4:Yb,Er/CdS and NaYF4:Yb,Er/CdS-380 show spectral characteristics similar to those of their individual components (CdS and CdS-380), but the PL intensities of the composites are higher, especially for NaYF4:Yb,Er/CdS-380. The annealing temperature-dependent PL spectra of NaYF4:Yb,Er/CdS reveal that all annealed samples exhibit significantly higher emission intensities compared to the pristine NaYF4:Yb,Er/CdS. Among these, NaYF4:Yb,Er/CdS-380 shows the weakest emission peak, which correlates with its lowest absorbance in the defect-related absorption tail. The annealing process in an argon atmosphere results in the loss of sulfur atoms from CdS, leading to the creation of sulfur vacancies. These vacancies introduce electronic states at the lower edge of the CdS conduction band. As the annealing temperature increases, the number of sulfur vacancies increases, which in turn enhances the PL emission due to the electronic states associated with these vacancies.

Annealing at 380 °C resulted in a significant boost in photocatalytic activity, with CdS and NaYF4:Yb,Er/CdS showing increases of 5.1 and 59.7 times, respectively, under $\lambda > 400$ nm light irradiation. The large difference in these enhancements—nearly an order of magnitude—emphasizes the importance of the strong interfacial interaction between NaYF4:Yb,Er and CdS in enhancing the photocatalytic performance of the NaYF4:Yb,Er/CdS-380 composite. The annealing process promotes phase transformation and improves interfacial bonding between NaYF4:Yb,Er and CdS. It also facilitates the formation of sulfur vacancies, as indicated by the changes observed in the light absorption and PL spectra. However, when the concentration of sulfur vacancies becomes too high, it leads to an increase in the recombination of photogenerated charge carriers, which ultimately reduces the photocatalytic H_2 evolution activity. This trend is particularly evident in the NaYF4:Yb,Er/CdS-450 sample, where a higher density of sulfur vacancies corresponds to a marked decrease in activity [1].

6.2. Photocatalyst Characterization

XPS, FTIR, and DFT calculations confirmed the presence of a strong electronic coupling between CdS and $ZnIn_2S_4$. These synthesized CdS/$ZnIn_2S_4$ heterojunctions showed enhanced photocatalytic water-splitting performance compared to pristine CdS [49]. In the study [3], CN and PCN were successfully synthesized by a facile calcination method and their composites were prepared with P25. All the synthesized photocatalysts were thoroughly characterized by XRD, FTIR, Raman spectroscopy, UV–visible DRS, FESEM and LRTEM-HRTEM techniques. These results are additionally confirmed by comprehensive characterizations, such as XRD, FT-IR, TEM, SEM, BET, UV–vis DRS, XPS, photoelectric performance measurements, and steady-state/transient fluorescence analyses [56].

In general, composite materials are extensively characterized using various techniques, including X-ray diffraction (XRD), Fourier-transform infrared spectroscopy (FTIR),

scanning electron microscopy (SEM), Brunauer–Emmett–Teller (BET) surface area analysis, X-ray photoelectron spectroscopy (XPS), vibrating sample magnetometry (VSM), ultraviolet–visible diffuse reflectance spectroscopy (UV–Vis/DRS), photoluminescence spectroscopy (PL) and electrochemical impedance spectroscopy (EIS) [47].

6.3. Durability and Recyclability of Selected Composite Materials

The photostability and recyclability of composite materials are key parameters for assessing their practical viability and are of crucial importance for large-scale hydrogen production [68]. Photostability is usually evaluated by longevity under irradiation, expressed in hours of sustained activity, by structural integrity, determined by e.g., XRD, TEM and/or XPS before and after testing, or by the loss of activity over time. On the other hand, recyclability is usually assessed by the number of cycles before a significant drop in photoactivity, recovery efficiency or hydrogen yield after regeneration, depending on the regeneration method. However, it is important to point out that it is very difficult to compare the results published in the literature, as there are no standardized procedures. Therefore, the published results often refer to the comparison of composite materials that differ in their chemical composition or were produced using different synthesis methods, and their testing is often carried out under different operating conditions. Considering the above-mentioned, MOF- and COF-based composites probably exhibit the best photostability and recyclability, while the CdS- and perovskite-based photocatalysts are sensitive due to photocorrosion and exhibit phase instability.

The stability of PCN/Mo-2 was investigated by repeated photocatalytic H_2 evolution cycles without Pt co-catalyst. The H_2 evolution rate of PCN/Mo-2 remained linear and constant over four cycles, demonstrating its satisfactory stability in visible-light-driven photocatalytic H_2 evolution [2]. Four recycling experiments confirmed the stability of SCNO/CoO (0.2) and there no significant deactivation during the H_2 evolution, indicating its excellent potential for long-term sustainable use [7].

The H_2 evolution performance of BZF-5 remained stable over three cycles and showed only minimal changes. In a 7-h long-term photocatalytic test under visible light, BZF-5 showed good stability. These results confirm that the BZF-5 composite photocatalyst exhibits excellent photocatalytic performance and remarkable stability during extended H_2 evolution under visible light [42]. The CdS/ZIS-0.3 heterojunctions, revealed high photocatalytic activity even after six test cycles, demonstrating excellent long-term stability [49]. The Pd/SCN sample (10 h) was subjected to cyclic tests under the same conditions. After four cycles, the photocatalytic H_2 production rate remained high at 259 μmol/h, demonstrating excellent stability and sustained performance [58]. After four cycles, a slight decrease in photocatalytic H_2 production by M@T/ZIS-50 was observed, probably due to mass loss during the photocatalyst separation and recovery process [63].

There are several strategies, which are mostly based on coating technologies, that can be used to reduce the toxicity of the CdS- and perovskite-based composites while simultaneously maintaining or enhancing their photocatalytic performances for H_2 production. For this purpose, the following approaches are most commonly used: (i) encapsulation with protective coatings (e.g., carbon or polymer coating, SiO_2 or Al_2O_3 shell, etc.) to isolate toxic constituents, such as Cd^{2+} and similar components, from leaching into the environment; (ii) doping/alloying to replace toxic elements or passivate their release (e.g., Zn alloying in CdS, production of lead-free perovskites, etc.); and (iii) immobilization on stable substrates to fix the material on non-leachable supports (e.g., encapsulation of CdS in a MOF/COF matrix), etc.

7. Conclusions and Challenges

Photocatalytic H_2 production is a promising approach to tackle the global energy crisis and reduce dependence on fossil fuels. However, achieving high efficiency in this process remains a challenge due to persistent issues such as charge carrier recombination, narrow light absorption ranges, and material instability. The development of non-Pt photocatalysts and material modifications, including doping and heterojunction formation in materials like TiO_2, CoO and g-C_3N_4, is critical to improving performance. TiO_2 (P25) has demonstrated potential as a benchmark photocatalyst, but its limitations in charge separation and stability necessitate the development of next-generation materials that perform more efficiently. Materials such as g-C_3N_4 and CdS show promise but their low efficiency and environmental concerns still limit real application. To maximize the potential of photocatalytic H_2 production, overcoming these barriers is critical for scalability and economic viability. Optimizing the physicochemical properties, especially the electronic structures, of materials is key to developing efficient and cost-effective photocatalysts. Carbon-based materials, especially g-C_3N_4, are characterized by their non-toxic nature, stability, and ease of synthesis. Combining these materials with semiconductors to form heterojunctions or composites can improve charge separation and, thus, photocatalytic performance. In addition, the integration of advanced materials, such as metal–organic frameworks (MOFs) and covalent organic frameworks (COFs), can further enhance photocatalytic efficiency due to their tunable properties and stability.

Recent advances in photocatalytic H_2 production, such as the integration of materials like phosphorus-doped graphitic carbon nitride (PCN), CoO quantum dots, and MoO_{3-x}, have led to significant improvements in efficiency. These improvements are largely due to better charge carrier separation, increased stability, and expanded light absorption. For example, the coupling of PCN with TiO_2 (P25) has improved its electrical conductivity and photocatalytic performance, leading to higher H_2 production. Similarly, the incorporation of CoO quantum dots into g-C_3N_4 hollow spheres has enabled improved charge separation, which has increased photocatalytic efficiency. Despite these advancements, challenges remain in optimizing charge carrier dynamics and material stability. Nonmetallic elements, such as boron in $CoMoO_4$, have improved photocatalytic performance, but high recombination rates and insufficient oxidation capacity are still limiting factors. The use of MoS_2 and MXenes in semiconductor composites has shown improved charge transfer and photocatalytic efficiency and is a promising alternative to platinum-based systems. However, there are still stability and scalability issues with these materials. For example, excessive loading of Ti_3C_2 can block the active sites and reduce photocatalytic performance, while the reactivity of the material in an aqueous environment can lead to decomposition. The scalability of synthesis methods for materials such as MXenes and MoS_2 composites remains a major hurdle. Large-scale production is not yet cost-effective, and the stability of these materials over time needs further investigation. The integration of sustainable materials, including MoS_2 and MXenes, plays a critical role in reducing dependence on precious metals such as platinum, thereby reducing costs and increasing the economic viability of photocatalytic H_2 production.

Further research should focus on improving the scalability and long-term stability of photocatalytic systems. Optimization of material loading, heterojunction design and composite interfaces will be crucial for maximizing photocatalytic efficiency. In addition, structural modifications of semiconductor materials, such as those observed in Ti3C2–TiO2 composites, are crucial for improving light absorption and charge separation. Ultimately, the development of photocatalysts that maintain high stability, recyclability, and efficiency over long periods of time is essential for practical large-scale H_2 production. With continued

innovation and refinement, these materials have the potential to revolutionize sustainable H_2 production and contribute to the transition to renewable energy sources.

Author Contributions: A.B. and V.T. contributed equally to this work. All authors have read and agreed to the published version of the manuscript.

Funding: This research received no external funding.

Conflicts of Interest: The authors declare no conflicts of interest.

References

1. Zhu, H.; Yang, Y.; Kang, Y.; Niu, P.; Kang, X.; Yang, Z.; Ye, H.; Liu, G. Strong interface contact between $NaYF_4$:Yb, Er and CdS promoting photocatalytic hydrogen evolution of $NaYF_4$:Yb,Er/CdS composites. *J. Mater. Sci. Technol.* **2022**, *102*, 1–7. [CrossRef]
2. Zhu, S.; Zhao, Z.; Zhou, J.; Wang, Y.; Wang, W.; Li, T. Natural molybdenite mineral enhanced polymeric carbon nitride nano-composites for efficient noble-metal-free photocatalytic hydrogen evolution. *Mater. Res. Bull.* **2021**, *136*, 111158.
3. Wadhai, S.; Jadhav, Y.; Thakur, P. Synthesis of metal-free phosphorus doped graphitic carbon nitride-P25 (TiO_2) composite: Characterization, cyclic voltammetry and photocatalytic hydrogen evolution. *Sol. Energy Mater. Sol. Cells* **2021**, *223*, 110958. [CrossRef]
4. Ren, G.; Ren, Q.; Ren, Z.; Chen, P.; Yue, M.; Sun, N.; Gao, J.; Wu, J.; Fu, Y.; Ma, J. Laser solid-phase synthesis of TiO_2 anatase/rutile homojunctions for efficient photocatalytic hydrogen evolution. *Opt. Express* **2025**, *33*, 13692. [CrossRef]
5. Suhaimi, N.H.S.; Azhar, R.; Adzis, N.S.; Ishak, M.A.M.; Ramli, M.Z.; Hamzah, M.Y.; Ismail, K.; Nawawi, W.I. Recent updates on TiO_2-based materials for various photocatalytic applications in environmental remediation and energy production. *Desalin. Water Treat.* **2025**, *321*, 100976. [CrossRef]
6. Christoforidis, K.C.; Fornasiero, P. Photocatalytic hydrogen production: A rift into the future energy supply. *ChemCatChem* **2017**, *9*, 1523–1544. [CrossRef]
7. Ying, H.; Huang, Z.; Dong, G.; Ying, H.; Huang, Z.; Dong, G.; Zhang, Y. The charge transfer pathway of CoO QDs/g-C_3N_4 composites for highly efficient photocatalytic hydrogen evolution. *J. Photoch. Photobiol. A Chem.* **2021**, *415*, 113305. [CrossRef]
8. Wang, J.-T.; Liu, G.-F.; Yu, K.; Liu, H.-H.; Zhang, Q.; Pan, J.; Wei, Q.; Wei, L. Photocatalytic hydrogen evolution on CdS–based composites derived from in situ carbonization of a sulfonic azo dye complex. *Inorg. Chem. Commun.* **2021**, *125*, 108370. [CrossRef]
9. Hu, S.; Ma, L.; You, J.; Li, F.; Fan, Z.; Lu, G.; Liu, D.; Gui, J. Enhanced visible light photocatalytic performance of g-C_3N_4 photocatalysts co-doped with iron and phosphorus. *Appl. Surf. Sci.* **2014**, *311*, 164–171. [CrossRef]
10. Singh, J.A.; Overbury, S.H.; Dudney, N.J.; Li, M.; Veith, G.M. Gold nanoparticles supported on carbon nitride: Influence of surface hydroxyls on low temperature carbon monoxide oxidation. *ACS Catal.* **2012**, *2*, 1138–1146. [CrossRef]
11. Ge, L.; Han, C.; Liu, J. Novel visible light-induced g-C_3N_4/Bi_2WO_6 composite photocatalysts for efficient degradation of methyl orange. *Appl. Catal. B Environ.* **2011**, *109*, 100–107. [CrossRef]
12. Yan, J.; Wu, H.; Chen, H.; Zhang, Y.; Zhang, F.; Liu, S.F. Fabrication of TiO_2/C_3N_4 heterostructure for enhanced photocatalytic Z-scheme overall water splitting. *Appl. Catal. B Environ.* **2016**, *191*, 130–137. [CrossRef]
13. Hernández-Alonso, M.D.; Portela, R.; Coronado, J.M. Turning sunlight into fuels: Photocatalysis for energy. In *Design of Advanced Photocatalytic Materials for Energy and Environmental Applications*; Green Energy and Technol; Coronado, J.M., Ed.; Springer: London, UK, 2013; Chapter 4; pp. 75–98.
14. Heinzel, A.; Vogel, B.; Hübner, P. Reforming of natural gas—Hydrogen generation for small scale stationary fuel cell systems. *J. Power Sources* **2002**, *105*, 202–207. [CrossRef]
15. Dash, S.K.; Chakraborty, S.; Elangovan, D. A brief review of hydrogen production methods and their challenges. *Energies* **2023**, *16*, 1141. [CrossRef]
16. Manzoor, M.F.; Ahmed, E.; Ahmad, M.; Manzoor, M.F.; Ahmed, E.; Ahmad, M.; Ahmad, I.; Rana, A.M.; Ali, A.; Ghouri, M.I.; et al. Enhanced photocatalytic activity of hydrogen evolution through Cu incorporated ZnO nano composites. *Mater. Sci. Semicond. Process.* **2020**, *120*, 105278. [CrossRef]
17. Hernández-Alonso, M.D.; Fresno, F.; Suárez, S.; Coronado, J.M. Development of alternative photocatalysts to TiO_2: Challenges and opportunities. *Energy Environ. Sci.* **2009**, *2*, 1231–1257. [CrossRef]
18. Ding, F.; Yang, D.; Tong, Z.; Nan, Y.; Wang, Y.; Zou, X.; Jiang, Z. Graphitic carbon nitride-based nanocomposites as visible-light driven photocatalysts for environmental purification. *Environ. Sci. Nano* **2017**, *4*, 1455–1469. [CrossRef]
19. Bhanderi, D.; Lakhani, P.; Modi, C.K. Graphitic carbon nitride (g-C_3N_4) as an emerging photocatalyst for sustainable environmental applications: A comprehensive review. *RSC Sustain.* **2024**, *2*, 265–287. [CrossRef]
20. Qiao, S.; Di, M.; Jiang, J.-X.; Han, B.-H. Conjugated porous polymers for photocatalysis: The road from catalytic mechanism, molecular structure to advanced applications. *EnergyChem* **2022**, *4*, 100094. [CrossRef]
21. Low, J.; Yu, J.; Jaroniec, M.; Wageh, S.; Al-Ghamdi, A.A. Heterojunction photocatalysts. *Adv. Mater.* **2017**, *29*, 1601694. [CrossRef]

22. Sohail, M.; Rauf, S.; Irfan, M.; Hayat, A.; Alghamdi, M.M.; El-Zahhar, A.A.; Ghernaout, D.; Al-Hadeethi, Y.; Lv, W. Recent developments, advances and strategies in heterogeneous photocatalysts for water splitting. *Nanoscale Adv.* **2024**, *6*, 1286–1330. [CrossRef] [PubMed]
23. Balapure, A.; Dutta, J.R.; Ganesan, R. Recent advances in semiconductor heterojunctions: A detailed review of the fundamentals of photocatalysis, charge transfer and materials. *RSC Appl. Interfaces* **2024**, *1*, 43–69. [CrossRef]
24. Li, K.; Gao, S.; Wang, Q.; Xu, H.; Wang, Z.; Huang, B.; Dai, Y.; Lu, J. In-Situ-Reduced Synthesis of Ti^{3+} Self-Doped TiO_2/g-C_3N_4 Heterojunctions with High Photocatalytic Performance under LED Light Irradiation. *ACS Appl. Mater. Interfaces* **2015**, *7*, 9023–9030. [CrossRef] [PubMed]
25. Huang, L.Y.; Xu, H.; Li, Y.P.; Cheng, X.; Xia, J.; Xu, Y.; Cai, G. Visible-light-induced WO_3/g-C_3N_4 composites with enhanced photocatalytic activity. *Dalton Trans.* **2013**, *42*, 8606. [CrossRef]
26. Pan, C.; Xu, J.; Wang, Y.; Li, D.; Zhu, Y. Dramatic activity of C_3N_4/$BiPO_4$ photocatalyst with core/shell structure formed by self-assembly. *Adv. Funct. Mater.* **2012**, *22*, 1518. [CrossRef]
27. Che, L.; Pan, J.; Cai, K.; Cong, Y.; Lv, S.-W. The construction of p-n heterojunction for enhancing photocatalytic performance in environmental application: A review. *Sep. Purif. Technol.* **2023**, *315*, 123708. [CrossRef]
28. Fernández-Catalá, J.; Greco, R.; Navlani-García, M.; Cao, W.; Berenguer-Murcia, Á.; Cazorla-Amorós, D. g-C_3N_4-based direct Z-scheme photocatalysts for environmental applications. *Catalysts* **2022**, *12*, 1137. [CrossRef]
29. Zhang, J.; Hu, Y.; Jiang, X.; Chen, S.; Meng, S.; Fu, X. Design of a direct Z-scheme photocatalyst: Preparation and characterization of Bi_2O_3/g-C_3N_4 with high visible light activity. *J. Hazard. Mater.* **2014**, *280*, 713–722. [CrossRef]
30. Omidkar, A.; Hu, J.; Chen, Z. p-n heterojunction of nickel oxide on titanium dioxide nanosheets for hydrogen and value-added chemicals coproduction from glycerol photoreforming. *J. Colloid Interface Sci.* **2023**, *647*, 255–263.
31. Maeda, K. Z-scheme water splitting using two different semiconductor photocatalysts. *ACS Catal.* **2013**, *3*, 1486–1503. [CrossRef]
32. Marschall, R. 50 years of materials research for photocatalytic water splitting. *Eur. J. Inorg. Chem.* **2021**, *14*, 2435–2441. [CrossRef]
33. Liu, X.; Zhang, Q.; Ma, D. Advances in 2D/2D Z-scheme heterojunctions for photocatalytic applications. *Solar RRL* **2021**, *5*, 2000397. [CrossRef]
34. Li, X.; Garlisi, C.; Guan, Q.; Anwer, S.; Al-Ali, K.; Palmisano, G.; Zheng, L. A review of material aspects in developing direct Z-scheme photocatalysts. *Mater. Today* **2021**, *47*, 75–107. [CrossRef]
35. Xu, Q.; Zhang, L.; Yu, J.; Wageh, S.; Al-Ghamdi, A.A.; Jaroniec, M. Direct Z-scheme photocatalysts: Principles, synthesis, and applications. *Mater. Today* **2018**, *21*, 1042–1063. [CrossRef]
36. Zhou, F.Q.; Fan, J.C.; Xu, Q.J.; Min, Y.L. BiVO4 nanowires decorated with CdS nanoparticles as a Z-scheme photocatalyst with enhanced H_2 generation. *Appl. Catal. B Environ.* **2017**, *201*, 77–83. [CrossRef]
37. Xu, Q.; Zhang, L.; Cheng, B.; Fan, J.; Yu, J. S-scheme heterojunction photocatalyst. *Chem* **2020**, *6*, 1543–1559. [CrossRef]
38. Liu, J.; Chen, L.; Cui, H.; Zhang, J.; Zhang, L.; Su, C.-Y. Applications of metal–organic frameworks in heterogeneous supramolecular catalysis. *Chem. Soc. Rev.* **2014**, *43*, 6011–6061. [CrossRef]
39. Gao, Z.; Wang, L.; Wang, L.; Huang, J.; She, H.; Wang, Q. Construction of heterostructured g-C_3N_4@TiATA/Pt composites for efficacious photocatalytic hydrogen evolution. *Int. J. Hydrogen Energy* **2019**, *44*, 24407–24417. [CrossRef]
40. You, J.; Zhao, Y.; Wang, L.; Bao, W. Recent developments in the photocatalytic applications of covalent organic frameworks: A review. *J. Clean. Prod.* **2021**, *291*, 125822. [CrossRef]
41. Yi, J.; Zhang, L.; Wang, W.; Yi, Q.; Wu, H.; Li, J.; Guo, J. Constructing the covalent organic framework and In_2O_3 composites via covalent bonds towards excellent visible-light photocatalytic hydrogen evolution. *Fuel* **2024**, *355*, 129470. [CrossRef]
42. Gao, H.; Zhang, P.; Zhao, J.; Zhang, Y.; Hu, J.; Shao, G. Plasmon enhancement on photocatalytic hydrogen production over the Z-scheme photosynthetic heterojunction system. *Appl. Catal. B Environ.* **2017**, *210*, 297–305. [CrossRef]
43. Gu, H.; Liu, C.; Zhu, J.; Gu, J.; Wujcik, E.K.; Shao, L.; Wang, N.; Wei, H.; Scaffaro, R.; Zhang, J.; et al. Introducing advanced composites and hybrid materials. *Adv. Compos. Hybrid Mater.* **2018**, *1*, 1–5. [CrossRef]
44. Lu, H.; Jia, R.; Wang, C.; Guan, W.; Wang, P.; Zhang, L.; Gan, Z.; Dong, L.; Yu, L.; Sui, L. High efficiency photocatalytic hydrogen evolution by black phosphorus quantum dots decorated 1D g-C_3N_4 nanotubes. *Int. J. Hydrogen Energy* **2024**, *95*, 766–772. [CrossRef]
45. Augustin, A.; Yesupatham, M.S.; Dhileepan, M.D.; Son, S.; Ravindran, E.; Neppolian, B.; Kim, H.; Sekar, K. Construction of organic–inorganic hybrid composites derived from C_3N_5 incorporated with CeO_2 for enhanced photocatalytic hydrogen evolution. *Energy Adv.* **2024**, *3*, 2604–2612. [CrossRef]
46. Huang, Z.; Liu, J.; Zong, S.; Wang, X.; Chen, K.; Liu, L.; Fang, Y. Fabrication of graphitic carbon Nitride/Nonstoichiometric molybdenum oxide nanorod composite with the nonmetal plasma enhanced photocatalytic hydrogen evolution activity. *J. Colloid Interface Sci.* **2022**, *606*, 848–859. [CrossRef]
47. Chen, D.; Wang, X.; Zhang, X.; Yang, Y.; Xu, Y.; Qian, G. Facile fabrication of mesoporous biochar/$ZnFe_2O_4$ composite with enhanced visible-light photocatalytic hydrogen evolution. *Int. J. Hydrogen Energy* **2019**, *44*, 19967–19977. [CrossRef]

48. Xie, L.; Teng, J.; Li, T.; Li, F. Z-type heterojunction Pt/$Zn_{0.2}Cd_{0.8}S$/$Cs_3PW_{12}O_{40}$ Mitigating photocorrosion, leveraging photochromism, and efficient photocatalytic hydrogen evolution. *J. Colloid Interface Sci.* **2025**, *679 Pt B*, 114–123. [CrossRef] [PubMed]
49. Li, P.; Liu, M.; Li, J.; Guo, J.; Zhou, Q.; Zhao, X.; Wang, S.; Wang, L.; Wang, J.; Chen, Y.; et al. Atomic heterojunction-induced accelerated charge transfer for boosted photocatalytic hydrogen evolution over 1D CdS nanorod/2D $ZnIn_2S_4$ nanosheet composites. *J. Colloid Interface Sci.* **2021**, *604*, 500–507. [CrossRef]
50. Chen, K.; Liu, J.; Huang, Z.; Zong, S.; Liu, L.; Tan, W. Construction of novel 2D-0D $MnPS_3$–$Cs_4W_{11}O_{35}$ composite for the improved photocatalytic hydrogen evolution activity. *Int. J. Hydrogen Energy* **2021**, *46*, 33823–33834. [CrossRef]
51. Li, Q.; Xu, J.; Shang, Y. The photocatalytic hydrogen evolution activity enhanced by doping nonmetallic B and constructing interfacial p-n heterojunction to co-regulate photogenerated carrier migration. *J. Alloys Compd.* **2025**, *1010*, 177485. [CrossRef]
52. Chang, S.; Gu, H.; Zhang, H.; Wang, X.; Li, Q.; Cui, Y.; Dai, W.-L. Facile construction of a robust CuS@$NaNbO_3$ nanorod composite: A unique p-n heterojunction structure with superior performance in photocatalytic hydrogen evolution. *J. Colloid Interface Sci.* **2023**, *644*, 304–314. [CrossRef] [PubMed]
53. Fang, N.; Yan, P.; Koide, R.; Shu, S.; Chu, Y.; Wang, Z.; Sano, T. A novel $Co_{1.29}Ni_{1.71}O_4$/glycerolate-derived oxygen-vacancies-containing TiO_2 composite for highly efficient photocatalytic hydrogen evolution. *J. Environ. Chem. Eng.* **2023**, *11*, 109142. [CrossRef]
54. Li, H.; Wang, G.; Zhang, X.; Jin, Z. Based on amorphous carbon C@ZnxCd1-xS/Co_3O_4 composite for efficient photocatalytic hydrogen evolution. *Int. J. Hydrogen Energy* **2020**, *45*, 8405–8417. [CrossRef]
55. Wu, T.; Huang, J.; Cheng, G.; Pang, Y. Enhanced photocatalytic hydrogen evolution based on ternary noble-metal-free Co_3O_4/CdS/g-C_3N_4 composite. *Mater. Lett.* **2021**, *292*, 129274. [CrossRef]
56. Zhang, L.; Hao, X.; Li, Y.; Jin, Z. Performance of WO_3/g-C_3N_4 heterojunction composite boosting with NiS for photocatalytic hydrogen evolution. *Appl. Surf. Sci.* **2020**, *499*, 143862. [CrossRef]
57. Xu, J.; Qi, Y.; Wang, W.; Wang, L. Montmorillonite-hybridized g-C_3N_4 composite modified by NiCoP cocatalyst for efficient visible-light-driven photocatalytic hydrogen evolution by dye-sensitization. *Int. J. Hydrogen Energy* **2019**, *44*, 4114–4122. [CrossRef]
58. Huang, Z.; Zhang, Y.; Dai, H.; Wang, Y.; Qin, C.; Chen, W.; Zhou, Y.; Yuan, S. Highly dispersed Pd nanoparticles hybridizing with 3D hollow-sphere g-C3N4 to construct 0D/3D composites for efficient photocatalytic hydrogen evolution. *J. Catal.* **2019**, *378*, 331–340. [CrossRef]
59. Huang, T.; Huang, Z.; Yang, X.; Yang, S.; Gao, Q.; Cai, X.; Liu, Y.; Fang, Y.; Zhang, S.; Zhang, S. Green and regulable synthesis of CdNCN on CdS semiconductor: Atomic-level heterostructures for enhanced photocatalytic hydrogen evolution. *Adv. Powder Mater.* **2024**, *3*, 100242. [CrossRef]
60. Yang, X.; Barwani, S.A.; Alhabradi, M.; Alruwaili, M.; Saremi-Yarahmadi, S.; Clarkson, T.; Roy, A.; Shanks, K.; Chang, H.; Tahir, A.A. Synthesis, characterization, and photocatalytic hydrogen evolution performance of neodymium iron composites: Influence of annealing temperature. *Inorg. Chem. Commun.* **2023**, *158 Pt 1*, 111592. [CrossRef]
61. Zheng, S.; Peng, S.; Wang, Z.; Huang, J.; Luo, X.; Han, L.; Li, X. Schottky-structured 0D/2D composites via electrostatic self-assembly for efficient photocatalytic hydrogen evolution. *Ceram. Int.* **2021**, *47*, 28304–28311. [CrossRef]
62. Li, Q.; Zhang, H.; Gu, H.; Cui, Y.; Gao, R.; Dai, W.-L. In situ Growth of $Cd_{0.5}Zn_{0.5}S$ Nanorods on Ti_3C_2 MXene Nanosheet for Efficient Visible-Light-Driven Photocatalytic Hydrogen Evolution. *Acta Phys. Chim. Sin.* **2024**, *40*, 100031. [CrossRef]
63. Huang, K.; Li, C.; Meng, X. In-situ construction of ternary Ti_3C_2 MXene@TiO_2/$ZnIn_2S_4$ composites for highly efficient photocatalytic hydrogen evolution. *J. Colloid Interface Sci.* **2020**, *580*, 669–680. [CrossRef] [PubMed]
64. Zong, S.; Liu, J.; Huang, Z.; Liu, L.; Liu, J.; Zheng, J.; Fang, Y. Mxene-TiO_2 composite with exposed {101} facets for the improved photocatalytic hydrogen evolution activity. *J. Alloys Compd.* **2022**, *896*, 163039. [CrossRef]
65. Meng, F.; Qin, Y.; Lu, J.; Lin, X.; Meng, M.; Sun, G.; Yan, Y. Biomimetic design and synthesis of visible-light-driven g-C_3N_4 nanotube @polydopamine/NiCo-layered double hydroxides composite photocatalysts for improved photocatalytic hydrogen evolution activity. *J. Colloid Interface Sci.* **2021**, *584*, 464–473. [CrossRef] [PubMed]
66. Zhang, Q.; Li, G.; Bai, J.; He, R.; Li, C. Enhanced photocatalytic activities of CdS-BiOCl/PAN composites towards photocatalytic hydrogen evolution. *Mater. Res. Bull.* **2019**, *117*, 9–17. [CrossRef]
67. Wang, F.; Liu, X. Recent advances in the chemistry of lanthanide-doped upconversion nanocrystals. *Chem. Soc. Rev.* **2009**, *38*, 976–989. [CrossRef]
68. Zhang, M.; Piao, C.; Wang, D.; Liu, Z.; Liu, J.; Zhang, Z.; Wang, J.; Song, Y. Fixed Z-scheme TiO_2 | Ti | WO_3 composite film as recyclable and reusable photocatalyst for highly effective hydrogen production. *Opt. Mater.* **2020**, *99*, 109545. [CrossRef]

Disclaimer/Publisher's Note: The statements, opinions and data contained in all publications are solely those of the individual author(s) and contributor(s) and not of MDPI and/or the editor(s). MDPI and/or the editor(s) disclaim responsibility for any injury to people or property resulting from any ideas, methods, instructions or products referred to in the content.